Ernest Chi Fru
Senior Lecturer in Geomicrobiology
Earth and Ocean Sciences
Cardiff University
CF10 4AT Cardiff, UK
Email: ChiFruE@cardiff.ac.uk
02/04/2018

Dear Dr Samankassou,

Thank you immensely for editing our paper, *Sedimentary mechanisms of a modern banded iron formation on Milos Island, Greece*, which is currently in revision for final publication in Solid Earth.
I have gone through the manuscript to effect the minor changes you recommended. I am therefore delighted to resubmit the revised version of the manuscript for your consideration, hoping that you will find the changes adequate to consider our paper suitable for final publication in Solid Earth.

Thank you very much for your time.

Kind regards,
Ernest

Sedimentary mechanisms of a modern banded iron formation on Milos Island, Greece

[1,2]Ernest Chi Fru*, [3]Stephanos Kilias, [4,5]Magnus Ivarsson, [1]Jayne E. Rattray, [3]Katerina Gkika, [2]Iain McDonald, [6]Qian He, [1]Curt Broman

[1]Department of Geological Sciences, 10691, Stockholm University, Sweden.

[2]School of Earth and Ocean Sciences, Cardiff University, Park Place, CF10 3AT, Cardiff, UK.

[3]Department of Economic Geology and Geochemistry, Faculty of Geology and Geoenvironment, National and Kapodistrian University of Athens, Panepistimiopolis, Zographou, 15784, Athens, Greece.

[4]Department of Biology, University of Southern Denmark, Campusvej 55, Odense M, DK5230, Denmark

[5]Department of Palaeobiology, Swedish Museum of Natural History, Box 50007, Stockholm, Sweden.

[6]School of Chemistry, Cardiff University, Park Place, CF10 3AT, Cardiff, UK.

*Corresponding author

Tel: +44(0) 29 208 70058

Email: ChiFruE@cardiff.ac.uk

Short title: A modern banded iron formation

Abstract. An Early Quaternary shallow submarine hydrothermal iron formation (IF) in the Cape Vani sedimentary basin (CVSB) on Milos Island, Greece, displays banded rhythmicity similar to Precambrian banded iron formation (BIF). Field-wide stratigraphic and biogeochemical reconstruction show two temporal and spatially isolated iron deposits in the CVSB with distinct sedimentological character. Petrographic screening suggests the photoferrotrophic-like microfossil-rich IF (MFIF), accumulated on a basement consisting of andesites, in a ~150 m wide basin, in the SW margin of the basin. A banded non-fossiliferous IF (NFIF) sits on top of the Mn-rich sandstones at the transition to the renowned Mn-rich formation, capping the NFIF unit. Geochemical data relates the origin of the NFIF to periodic submarine volcanism and water column oxidation of released Fe(II) in conditions predominated by anoxia, similar to the MFIF. Raman spectroscopy pairs hematite-rich grains in the NFIF with relics of a carbonaceous material carrying an average $\delta^{13}C_{org}$ signature of ~-25‰. A similar $\delta^{13}C_{org}$ signature in the MFIF could not be directly coupled to hematite by mineralogy. The NFIF, which post dates large-scale Mn deposition in the CVSB, is composed primarily of amorphous Si (opal-$SiO_2 \cdot nH_2O$) while crystalline quartz (SiO_2) predominates the MFIF. An intricate interaction between tectonic processes, changing redox, biological activity and abiotic Si precipitation are proposed to have collectively formed the unmetamorphosed BIF-type deposits. Despite the differences in Precambrian ocean-atmosphere chemistry and the present geologic time, these formation mechanisms coincide with those believed to have formed Algoma-type BIFs proximal to active seafloor volcanic centers.

Keywords: Banded iron formation; BIF analog; Hydrothermal activity; Iron cycling; Silica cycling.

1 Introduction

Banded iron formations (BIFs) are marine sedimentary deposits formed predominantly during the Precambrian, containing at least 15% bulk Fe content and

Ernest C 29/3/2018 12:10
Deleted: Sedimentary and stratigraphic reconstruction, coupled to biogeochemical analysis and micro-nanoscale mineralogical characterization, hint that the Milos IF a modern BIF-type . Spatial coverage of the BIF-type rocks in relation to the economic grade Mn ore that brought prominence to the CVSB implicates tectonic activity and changing redox in their deposition.

Ernest Chi Fru 29/3/2018 09:49
Deleted: previously described

Ernest Chi Fru 29/3/2018 09:52
Deleted: strongly

Ernest Chi Fru 29/3/2018 09:53
Deleted: evidence

Ernest Chi Fru 29/3/2018 09:53
Deleted: apparently

Ernest Chi Fru 2/4/2018 16:22
Deleted: in a shallow submarine volcanic center

Fe-rich bands alternating with Si-rich layers (James, 1954; Gross, 1980; Simonson, 1985, 2003; Bekker et al., 2010). Recently, an Early Quaternary iron formation (IF), ~2.0 million years old and displaying banded rhythmicity typical of Precambrian banded iron formations (BIF), was serendipitously discovered in the Cape Vani sedimentary basin (CVSB) on Milos Island, Greece (Chi Fru et al., 2013, 2015). Before this discovery, Cape Vani was long known to host Mn oxide ores of economic potential (Hein et al., 2000; Liakopoulos et al., 2001; Glasby et al., 2005; Kilias et al., 2007).

Milos is an emergent volcano on the Hellenic Volcanic Arc (HVA) where arc-volcanism and seafloor hydrothermal activity occur in thinned pre-Alpine to Quaternary continental crust (Kilias et al., 2013b) (Fig. 1). The first reported IF from CVSB is unmetamorphosed and contains diverse microfossils encrusted by hematite, with ferrihydrite proposed as a primary precursor mineral (Chi Fru et al., 2013, 2015). Field stratigraphy, rare earth elements (REE), stable isotopes, petrographic and microfossil studies point to microbial Fe deposition in a semi-enclosed, shallow submarine basin under conditions analogous to those that formed the Precambrian Algoma-type BIFs near volcanic centers (Chi Fru et al., 2015). These earlier reports assumed a one-time basin-wide depositional event and a common origin for all Fe-rich sedimentary rocks in the CVSB.

However, it remains unclear what sedimentary processes caused the distinct deposition of the BIF-type rocks in a basin where Mn precipitation was apparently widespread at various intervals. Moreover, it is not known how the Mn ores relate temporally and spatially to Fe deposition in the ~1 km long CVSB. This knowledge may provide clues to processes that triggered large-scale deposition of similar Proterozoic Fe-Mn-rich deposits (Roy, 2006; Tsikos et al., 2010; Beukes et al., 2016).

Here, new sedimentological, petrological and biogeochemical analyses describe cycles of periodic precipitation of shallow submarine Si and Fe-rich sedimentary rocks and the plausible mechanisms that enabled their temporal and spatial separation from the Mn deposits in the CVSB. The data reveal a much more complex depositional system not only controlled by microbial Fe(II) oxidation as previously proposed (Chi Fru et al., 2013, 2015), but suggests episodic submarine hydrothermal activity coupled to changing redox conditions as a central mechanism in the formation of the banded iron rocks.

1.1 Geological setting

K-Ar radiometric dating of biotite and amphiboles belonging to the dacitic/andesitic lava domes flooring the CVSB basin gave an Upper Pliocene age of 2.38±0.1 Ma (Fytikas et al., 1986; Stewart and McPhie, 2006). The fossiliferous sandstones/sandy tuffs hosting the Mn-rich deposit, which contain the gastropod mollusk guide fossil, *Haustator biplicatus sp.* (Bronn, 1831), indicate an Upper Pliocene-Lower Pleistocene age. The geology, Fe and Mn mineralization of the CVSB have previously been described in detail (Plimer, 2000; Hein et al., 2000; Liakopoulos et al., 2001; Skarpelis and Koutles, 2004; Glasby et al., 2005; Stewart and McPhie, 2006; Kilias, 2011; Alfieris and Voudouris, 2005; Alfieris, 2006; Alfieris et al., 2013: Chi Fru et al., 2013, 2015; Papavassiliou et al., 2017). Briefly, the Milos IF is part of the CVSB, a recently emergent sedimentary rift basin located NW of Milos Island, along the HVA in the Aegean Sea, Greece (Fig. 1). It hosts a fossil analog of active shallow-submarine hydrothermal activity on the coast of Milos Island (Dando et al., 1995). The CVSB developed within a shallow-submarine rhyolitic-dacitic volcanic center, filled up mainly by a ~35-50 m thick stratigraphic succession of

volcaniclastic/epiclastic sandstones and sandy tuffs spanning Upper Pliocene to Lower Pleistocene, 35-40% of which is hydrothermally mineralized by Mn oxides and barite (Hein et al., 2000; Liakopoulos et al., 2001; Skarpelis and Koutles, 2004; Papavassiliou et al., 2017). Sedimentologic and ichnologic data, including sedimentary structures, lamellibranch, echinoid and brachiopod fossils, the gastropod mollusk fossil, Haustator biplicatus (Bronn, 1831), and microbially induced sedimentary structures (e.g., Kilias, 2011), suggest that most of the CVSB sandstones/sandy tuffs hosting the Mn-rich deposit, are foreshore to shoreface shallow submarine deposits, formed at a maximum depth of 200 mbsl. Over the last 0.8 Myr, fluctuating water depths due to sea-level change of up to 120 m and volcanic edifice building, has resulted in tectonic uplift of ~250 m (Papanikolaou et al., 1990). The CVSB infill, currently 35 m above sea level, is tectonically bound by extrusive rhyolite to the north, framed by elevated andesitic-dacitic centres, with the Cape Vani and the Katsimoutis dacitic lava domes being the most prominent (Fig. 1).

2 Methodology

2.1 Sample preparation

Prior to mineralogical and geochemical analysis, exposed rock surface layers were sawn and removed. GeoTech Labs (Vancouver, Canada) produced doubly polished thin sections for mineralogical and textural analysis. Trace and rare earth element analysis was performed after digestion of powdered samples with a mixture of acids (HNO_3, HCl, HF) and heat until a clear solution was obtained (Chi Fru et al., 2013, 2015).

2.2 Mineralogical analysis

156 **2.2.1 X-Ray Diffraction (XRD) analysis**

157 A PANalytical Xpert-pro diffractometer at room temperature, 45 kV, 40 mA and
158 1.5406 Å wavelength and Cu-Kα radiation and Ni-filter, was used for Powder X-Ray
159 Diffraction (PXRD) analysis. Samples were analyzed between 5-80° in step sizes of
160 0.017° with continuous mode scanning step time of 50.1650 s while rotating.

161

162 **2.2.2 Raman spectroscopy**

163 Raman analysis was performed with a confocal laser Raman spectrometer (Horiba
164 instrument LabRAM HR 800), equipped with a multichannel air-cooled (-70°C) 1024
165 x 256 pixel charge-coupled device (CCD) array detector as previously described (Chi
166 Fru et al. 2013, 2015). Spectral resolution was ~0.3 cm^{-1}/pixel. Accuracy was
167 determined by a repeated silicon wafer calibration standard at a characteristic Raman
168 line of 520.7 cm^{-1}.

169

170 **2.2.3 Transmission electron microscopy**

171 Specimens for transmission electron microscopy (TEM) were prepared from the
172 crushed rock specimen powder. This was followed by dry-dispersal onto a 300 mesh
173 holey carbon TEM Cu grid. Microscopy was conducted using a JEOL 2100 TEM
174 with a LaB_6 source in the School of Chemistry, Cardiff University, operated at
175 200kV. The X-EDS analysis was performed with an Oxford Instrument SDD detector
176 X-Max^N 80 T.

177

178 **2.2.4 Scanning electron microscopy**

179 Scanning Electron Microscopy-Energy Dispersive Spectroscopy (SEM-EDS) analysis
180 was done on a FEI QUANTA FEG 650 ESEM. Images were captured at 5 kV and

EDS data collected at 20 kV, using an Oxford T-Max 80 detector (Oxford Instruments, UK). The analyses were performed in low vacuum to minimize surface charging of uncoated samples. EDS elemental maps were collected for 30 min or until the signal had stabilized, indicated by a clear distribution trend. The data were further processed with the Oxford Aztec software.

2.3 Geochemical analysis

2.3.1 Laser ablation ICP-MS and trace element analysis

Laser Ablation-Inductively Coupled Plasma-Mass Spectrometry (LA-ICP-MS) was performed at Cardiff University on polished thin sections. The LA-ICP-MS system comprised a New Wave Research UP213 laser system coupled to a Thermo X Series 2 ICP-MS. The laser was operated using a frequency of 10 Hz at pulse energy of ~5mJ for an 80μm diameter beam using lines drawn perpendicular to the layering and at a movement speed of 26 microns sec^{-1}. Samples were analyzed in time resolved analysis (TRA) mode using acquisition times of between 110 and 250 seconds; comprising a 20 second gas blank, 80-220 second ablation and 10 second washout. Dwell times varied from 2 msec for major elements to 35 msec for low abundance trace elements. Blank subtraction was carried out using the Thermo Plasmalab software before time resolved data were exported to Excel.

Separated and independently pulverized banded layers were digested by lithium borate fusion followed by major, trace and rare earth element (REE) analyses using ICP- Atomic Emission Spectrometry-Mass Spectrometry (ICP-AES-MS) and X-Ray Florescence (XRF) at Bureau Veritas (Ankara). Geochemical data were compared with previously published results for the more widely investigated Mn deposits (Hein et al., 2000; Liakopoulos et al., 2001; Glasby et al., 2005).

206

207 **2.3.2 Isotope analysis**

208 C, N and S isotopic composition for the pulverized samples was determined as
209 previously described (Chi Fru et al., 2013, 2015), following combustion in a Carlo
210 Erba NC2500 analyzer and analyzed in a Finnigan MAT Delta V mass spectrometer,
211 via a split interface to reduce gas volume. Reproducibility was calculated to be better
212 than 0.15‰ for $\delta^{13}C$ and $\delta^{15}N$ and 0.2‰ for $\delta^{34}S$. Total C and N concentrations were
213 determined simultaneously when measuring the isotope ratios. The relative error was
214 <1% for both measurements. For carbon isotopic composition of organic carbon,
215 samples were pre-treated with concentrated HNO_3 prior to analysis.

216

217 **2.4 Organic geochemistry analysis**

218 Lipid biomarker and compound specific $\delta^{13}C$ analyses were executed on powdered
219 samples of sectioned bands from which exposed surface layers had been removed.
220 Modern sediments from Spathi Bay, 36°40'N, 24°31'E, southeast of Milos Island,
221 collected by push coring at 12.5 m below the seafloor were freeze-dried prior to
222 extraction to aid the identification of potential syngenetic biomarkers in the
223 Quaternary rocks. Between 4-6 g of ground samples were ultrasonically extracted
224 using 3×Methanol, 3×(1:1) Methanol:Dichloromethane (DCM), and 3×DCM and
225 extracts were combined and dried under N_2. Samples were subsequently re-dissolved
226 in DCM then methylated following the method of Ichihara and Fukubayashi (2010).
227 The resulting residue was silylated using, 20 µl pyridine and 20 µl (N, O-
228 Bis(trimethylsilyl)trifluoroacetamide) BSTFA and heated at 60˚C for 15 min. Total
229 lipid extracts were analyzed using a Shimadzu QP 2010 Ultra gas chromatography
230 mass spectrometer (GC/MS). Separation was performed on a Zebron ZB-5HT column

231 (30 m x 0.25 mm x 0.10 µm) with a helium carrier gas flow at 1.5 ml min^{-1}. Samples
232 were injected splitless, onto the column at 40˚C with the subsequent oven temperature
233 program ramped to 180˚C at a rate of 15˚C min^{-1}, followed by ramping to 325˚C at a
234 rate of 4˚C min^{-1} and a final hold for 15 min. The MS was set to scan from 50 to 800
235 m/z with an event time of 0.70 sec and a scan speed of 1111 u/sec. All peaks were
236 background subtracted and identification confirmed using the NIST GC/MS library
237 and literature spectra. Contamination was not introduced into the samples, as blank
238 samples worked up concurrently with the rock fractions had results comparable to the
239 ethyl acetate instrument blank.
240
241 **2.5 Chemical weathering analysis**
242 Chemical index of alternation (CIA) was used to determine whether variations in
243 chemical weathering intensities would in addition to hydrothermal activity deliver
244 materials into the depositional basin from the continent, according to the
245 formula: $CIA = Al_2O_3/(Al_2O_3 + CaO + Na_2O + K_2O) \times 100$. Extensively
246 applied, the CIA index reveals subtle changes in weathering fluxes (Nesbit and
247 Young, 1982; Maynard, 1993; Bahlburg & Dobrzinski, 2011), where increasing CIA
248 values generally indicate amplified chemical dissolution of rocks and selective release
249 of dissolvable CaO, Na_2O and K_2O into solution (Nesbit & Young, 1982; Maynard,
250 1993; Bahlburg & Dobrzinski, 2011). The broken rock particles enriched in the
251 poorly soluble Al_2O_3 fraction, settle to the seafloor as weathered sediments carrying a
252 chemical composition different from the source. In the absence of chemical
253 dissolution, no net chemical change is expected in the composition of sediments
254 compared to source and thus a low CIA index. CIA indices for detritus of 0-55, 55-75
255 and >75, are considered unweathered, unweathered to slightly weathered and

256 weathered to highly weathered, respectively (Nesbit & Young, 1982; Maynard, 1993;
257 Bahlburg & Dobrzinski, 2011).
258
259 **2.6 Redox analysis**
260 Redox depositional conditions were evaluated using the sequential Fe extraction
261 redox proxy (Poulton and Canfield, 2005, 2011), combined with REE composition of
262 the sediment (Planavsky et al., 2010).
263
264 **2.6.1 REE redox analysis**
265 REE data obtained as described in section 2.3.1 were normalized with the North
266 American Shale Composite (NASC) to maintain consistency with previous studies in
267 which NASC-normalized REE data (SN) were reported for the Milos BIF-type rocks
268 (Chi Fru et al., 2013, 2015). The data were further normalized with the Post Archean
269 Australian Shale (PAAS) (McLennan, 1989) standard for comparative purposes,
270 according to Bau and Dulski (1996). Ce anomalies, calculated from Ce/Ce*
271 ($Ce_{(SN)}/0.5Pr_{(SN)} + 0.5La_{(SN)}$) and Pr/Pr* ($Pr_{(SN)}/0.5Ce_{(SN)} + 0.5Nd_{(SN)}$) values, were
272 considered significant when Ce/Ce* and Pr/Pr* were less than and greater than 1,
273 respectively (Bau and Dulski et al., 1996; Planavsky et al., 2010).
274
275 **2.6.2 Sequential iron extraction redox analysis**
276 This analysis was performed on three representative MFIF samples and the six
277 sectioned bands of a typical NFIF sample using the method developed by Poulton and
278 Canfield (2005) and data interpreted accordingly (e.g., Canfield and Poulton, 2005,
279 2011; Guilbaud et al. 2015; Sperling et al. 2015). Reagent blanks and geological
280 standards were used for data calibration.

3 Results

3.1 Lithostratigraphy

Sedimentary structures, grain-size trends, lateral facies variations, vertical stacking trends, and key stratigraphic surfaces form the basis for facies analysis. Field-wide sedimentological and lithostratigraphical mapping of the CVSB in the summer and fall of 2014 enabled the assessment of the lateral and vertical coverage of the Milos iron oxide-rich facies relative to the Mn-rich sandstones that dominate the Early Quaternary sedimentary basin (Fig. 2). Six stratigraphic sections, representing marine siliciclastic lithofacies sequences, were investigated along a ~1 km SW-NE trending portion of the CVSB infill (Supplementary Figs 1-7). Sequence stratigraphy was conducted on outcrops and vertical shafts and tunnels left behind by previous Mn mining activity. Two of those sections; Section A located at 36°44'17.85''N, 24°21'17.72''E and Section B located at 36°44'35.11''N, 24°21'11.25''E, contain stratigraphic units composed of layered, bedded, or laminated rocks that contain ≥15 % Fe, in which the Fe minerals are commonly interlayered with quartz or chert, in agreement with the definition of Precambrian BIFs (James, 1954; Gross, 1980; Bekker et al., 2010). These IFs are descriptively referred to here as microfossiliferous iron formation (MFIF) according to Chi Fru et al. (2013, 2015), and non-microfossiliferous iron formation (NFIF) (this study), respectively (Fig. 2). The MFIF and the NFIF occupy at most ~20% of the entire CVSB infill. The stratigraphy and sedimentary lithofacies are illustrated below, using lithofacies codes modified after Bouma (1962), Miall (1978, 1985), Lowe (1982), Mutti (1992) and Shanmugam (2016).

Further field stratigraphic survey revealed considerable lithologic variability within three fault-bounded volcanosedimentary sub-basins in the CVSB (Fig. 2), which for the sake of simplicity are referred to as Basin 1—host of the MFIF; Basin 2—host of economic grade Mn ore; and Basin 3—host of the NFIF (Fig. 2). Each section is framed by distinct marginal normal faults that strike in the NW-SE and NE-SW to NNE-SSW directions, distinguishable by distinct lateral sedimentary facies exhibiting unique vertical sequence stratigraphy (Fig. 2; Supplementary Figs 1-7). Faulting in the CVSB is related to major geographical activation of extensional structures at intervals that shaped Milos into a complex mosaic of neotectonic units (Papanikolaou et al., 1990; van Hinsbergen et al., 2004).

3.1.1 Section A (36°44'17.85''N, 24°21'17.72''E)

Informally known as "Little Vani", Section A is the type section containing the MFIF at the base. It crops out in the W-SW edge of the CVSB (Figs 1 & 2) as a ~6-7 m high cliff resting stratigraphically on submarine dacitic and andesitic lavas and domes. This section extends laterally in the N-NE direction for an estimated 300–500 m.

Lithologically, the MFIF comprises laminated and massive fine-grained red and white weathered ferruginous jaspelitic red chert layers (Chi Fru et al., 2013, 2015). The chert layers contain morphologically distinct Fe minerals dispersed in a fine-grained siliceous matrix (Fig. 3), marked by the notable absence of pyrite and an extremely low S content (Chi Fru et al., 2013, 2015). Layers are tabular and typically laterally continuous at scales of several meters, whereas wave and current structures (e.g., cross-lamination) are generally absent from the MFIF. The hematite-rich MFIF laminae (Table 1) are built by massive encrustation of anoxygenic photoferrotrophic-like microbial biofilms by precipitated Fe (Chi Fru et al., 2013). The base of the MFIF

outcrop, is visibly mineralized by black diffused bands/veins composed of Mn oxides (Fig. 4 & Table 1).

A markedly ferruginous 2-3 m-thick section immediately overlies the MFIF, comprising a distinct package of Fe-rich beds that transition up the section (Figs 4A & 5). The lower 1-2 m consist of fine-grained sandstone beds that are well to moderately sorted, containing a 20-40 cm thick portion dominated by plane parallel-laminated sandstone/sandy tuff, massive to plane parallel-laminated sandstone/sandy tuff, and massive sandstone/sandy tuff lithofacies (Fig. 5; Supplementary Fig. 1). The fabric of these Fe-rich sandstone facies consists of sub-angular to sub-rounded and 100–600 μm fine to medium-grained volcaniclastic K-feldspar grains, making up to 75% of the total rock, with variable amounts of quartz and clay mineral grains.

The latter are overlain by a ~1-1.5 m sequence of poorly-sorted tabular clast-supported pebble-to-cobble conglomerate beds with an erosional base, grading upward into coarse to medium-grained sandstone/sandy tuff beds, with alternating conglomerate cycles (Fig. 5), averaging 20-40 cm in thickness. The cobble/pebble conglomerate clasts include intraformational volcanic rocks (dacite, andesite), allochthonous volcaniclastic sandstone, and volcaniclastic microclasts (e.g. K-feldspar), cemented by hematite (Fig. 5; Chi Fru et al., 2013; Kilias et al., 2013a). Towards the westernmost edge of the “Little Vani” section, there is a facies change from the graded pebbly conglomerate/sandy tuff rhythms to a predominantly Fe-rich conglomerate bed (Fig. 6A), termed the conglomerate-hosted IF (CIF) in Chi Fru et al. (2015), with a maximum thickness of ~0.5 m and a cobble size range of ~10 cm. The Fe-rich conglomerate bed transitions upward into medium-grained pebbly reddish ferruginous sandstones with thin volcanic rock and sandstone pebble lenses. This, in turn, grades upwards into a very-fine-grained greenish glauconite-bearing plane

parallel-laminated sandstone to siltstone bed; characterized by soft-sediment deformation structures, such as flame structures, convolute bedding and lamination structures, loop bedding, load casts, and pseudonodules (Supplementary Figs 1-2).

The "Little Vani" section is eventually capped along an erosional surface by an overlying 1-2 m thick section dominated by medium to fine-grained and moderately to poorly-sorted reddish Fe-rich tabular sandstone beds, 10–40 cm thick, topped by patchy sub-cm to cm-thick Mn-rich sandstones (Fig. 5; Supplementary Figs 1-2). Dominant lithofacies of the Fe-rich sandstone cap include planar and hummocky cross-bedding, exhibiting bioturbation in places. The Fe-rich lithofacies cap is laterally discontinuous, thinning out basinwards towards the N-NE, and can be observed smoothly grading into a 1-2 m thick section composed of cm to sub-cm-thick Mn–rich volcaniclastic sandstone lithofacies, described below in Section B. No Fe-rich hydrothermal feeder veins are obvious in the MFIF. However, feeder veins and Mn horizons can be observed to truncate laminations in the MFIF, and up through the whole "Little Vani" section (e.g., Figs 4C & 5).

The MFIF rests directly on the submarine dacites-andesites that were deposited in a relatively shallow submarine environment (Stewart and McPhie, 2006). The fine-grained, finely laminated nature of the MFIF, and, the lack of evidence of current or wave structures (e.g., symmetric ripples or hummocky cross-stratification), coupled to the absence of volcanogenic detrital particles and intraclast breccia structures, indicate a low energy sedimentation environment, marked by negligible volcanic interference (e.g., Tice and Lowe, 2006; Konhauser et al., 2017). This interpretation is supported by the observed enrichment of Fe in the MFIF; a characteristic of relatively deeper water lithofacies (Konhauser et al., 2017). This view is compatible with the proposition that hematite enrichment in the MFIF was

under the control of photoferrotrophic biofilms (Chi Fru et al., 2013) known to thrive at lower light intensities (Kappler et al., 2005; Li et al., 2013; Konhauser et al., 2017). The quiet environmental conditions would have ensured the formation of such stable photoferrotrophic biofilms over extended periods of time that would have facilitated the oxidation of hydrothermally released Fe(II) and the depositon of Fe(III) minerals.

In the overlying sandstone-conglomerate facies, the presence of sedimentary structures indicative of wave action and currents (e.g. cross-stratification), that signify rapid deposition during a high energy event, are consistent with a switch to a shallow-submarine high energy environment (Stewart and McPhie, 2006; Chi Fru et al., 2015). This shift in depositional environments may have been controlled by a combination of submarine volcano-constructional processes, synvolcanic rifting and volcano-tectonic uplift known to have formed the CVSB (Papanikolaou et al., 1990; Stewart and McPhie, 2006).

3.2 Section B (36°44'35.11''N, 24°21'11.25''E)

This ~8-10 m thick fault-bounded stratigraphic section, here referred to as "Magnus Hill", is the type section that contains the NFIF (Figs 2 & 7; Supplementary Figs 3-4). Two lithostratigraphic units—a lower unit A and an upper unit B—are identified in this study. Unit A is made up of a lower sandstone facies that is ~4-5 m thick, dominated by a Mn-oxide cement, overlain by reddish brown Fe-rich massive sandstone beds (Fig. 8 & Supplementary Figs 3-4). The lower sandstone facies represents the host of the main economic grade Mn oxide ores in the CVSB. This constitutes part of a separate study devoted to the Mn ores and will not be dealt with further here. Unit B, ~5 m thick, unconformambly overlies unit A and comprises two distinct packages of beds that transition up section from brownish pebble

conglomerate layers (0.5-1.0 m thick), in contact with the very fine-grained NFIF deposit (Supplementary Fig. 8 & 9). The NFIF is capped by patchy cm-thick crustiform Mn oxides. Bifurcating feeder veins composed of barite, quartz and Mn-Fe-oxide minerals cut through the underlying sandstone beds (Supplementary Fig. 4).

The NFIF is composed of banded Fe-rich rocks (Fig. 7) exposed on the topmost part of "Magnus Hill". About 2-3 m thick, the NFIF consists of mm to sub-mm thick, dark grey and brown Fe-rich bands, interbanded with reddish brown Si-rich layers (Figs 7 & 9-11; Supplementary Figs 10-11). Sedimentary structures in the NFIF are predominantly characterized by rhythmic mm to sub-mm thick laminations (e.g., Fig. 7). The iron oxide-rich bands made up mainly of hematite (Table 1 & Fig. 10C) are typically composed of very fine-grained angular to sub-angular volcanic dust material (i.e., fine volcanic ash with particle size under 0.063 mm, K-feldspar, tridymite and cristobalite (Table 1) in an amorphous Si and crystalline hematite matrix (Fig. 12)). The predominantly amorphous Si-rich bands are typically planar, finely laminated and composed of microcrystalline to cryptocrystalline ferruginous chert.

The NFIF is directly overlain by a ~1 m thick laminated to massive well-indurated, nodular-pisolitic ironstone bed (Fig. 8A, C & D) that locally preserves a sub-horizontal fabric reflecting the bedding in the original sediment or contain various ferruginous clasts such as fragments, nodules, pisoliths, and ooliths set in a hematite-rich siliceous matrix (Fig. 8C). Scattered cm scale pisoliths display a crude concentric internal layering, characterized by open and vermiform voids filled by cauliflower-like Mn oxides overprint (Fig. 8D). The ferruginous NFIF lithofacies are interpreted to represent the deepest water deposits in the "Magnus Hill" section based on its very fine-grained sedimentary composition, fine laminations and a paucity of intraclast breccias. These, combined with the lack of evidence for wave and current-formed

Ernest Chi Fru 29/3/2018 10:57
Deleted: strongly

sedimentary structures (e.g., hummocky cross-stratification, trough and ripple cross-stratification), indicate quiet water low energy sedimentation, likely below wave base (Simonson and Hassler, 1996; Trendall, 2002; Krapež et al., 2003; Konhauser et al., 2017).

We interpret that each graded Fe oxide-rich band of the NFIF (Supplementary Fig. 9), represents an individual fallout deposit from a proximal pyroclastic eruption. This interpretation is supported by normal grading in fine volcanic ash content that reflects their likely origin as pyroclastic fallout deposits in an otherwise quiet water setting. For example, tridymite is a stable SiO_2 polymorph formed at low pressures of up to 0.4 GPa and at temperatures of ~870-1470 ^{o}C (Swamy et al., 1994; Morris et al., 2016). The coincidence of tridymite formation with silicic volcanism is in agreement with the widespread distribution of andesite, dacite and rhyolite lava domes in the CVSB. For example, vapour phase production of tridymite together with sanidine identified in this study (Fig. 10) and Fe oxides is principally associated with rhyolite ash flow (Breitkreuz, 2013; Galan et al., 2013). Similarly, Cristobalite is a SiO_2 polymorph associated with high temperature rhyolitic eruptions (Horwell et al., 2010). Finally, in situ carbonaceous laminations are absent, suggesting that benthic microbial mat growth had no influence on deposition of the NFIF. Ironstones overlying the NFIF are difficult to interpret with the existing data, but may represent supergene ferruginous duricrust formation resulting from subaerial weathering (Anand et al., 2002).

3.3 Geochemistry

3.3.1 Geochemistry of the individual Fe-rich and Si-rich bands

455 The SEM-EDS-electron micrographs of the NFIF thin sections reveal distinct Fe
456 bands and Si-rich layers alternating periodically with each other in a fine sediment
457 matrix as shown by the grain size (Figs 9 & 11 & Supplementary Figs 9-11). Laser
458 ablation ICP-MS line analysis indicates Si and Fe count intensities in the Milos BIF-
459 type rocks are comparable to the 2.5 Ga Precambrian BIF reference from the
460 Kuruman IF formation, Transvaal Supergroup, South Africa (Fig. 11). The laser
461 ablation ICP-MS data further show an inverse correlation between Fe and Si, the two
462 major elemental components of BIFs, irrespective of the thousands of millions of
463 years gap separating the Precambrian deposit from the recently formed Milos IF
464 formation.
465
466 **3.3.2 Mineralogy of the individual Fe-rich and Si-rich bands**
467 No other Fe(III)(oxyhydr)oxide minerals have been identified in the Cape Vani
468 Fe-rich facies different from hematite. Electron imaging of the NFIF Fe-rich bands
469 suggests Si, Al and K-rich phases are mostly associated with the volcaniclastic
470 material predominated by K-feldspar clasts (Fig. 9; Supplementary Figs 10 & 11). A
471 unique feature of the NFIF is that the hematite in the Fe-rich bands occurs in tight
472 association with a carbonaceous material (Fig. 10C), but not for the hematite in the
473 Fe-rich sandstones and in the MFIF. This is also the case for the CIF overlying the
474 MFIF. Hematite showing a fluffy texture and at times presenting as framboidal
475 particles, is sprinkled in the Si-rich cement containing traces of Al and K in the MFIF
476 rocks (Fig. 3). Lack of association of the framboidal-iron-rich particles with S,
477 following SEM-EDS analysis, rules out a pyrite affiliation and is consistent with the
478 non-sulfidic depositional model suggested by the sequential iron extraction redox
479 proxy (Fig. 13D). TEM analysis suggests platy nano-Fe oxide-rich particles

predominate in the NFIF and MFIF, confirmed by overlaid X-ray Energy Dispersive spectra taken from selected areas (Fig. 12) and consistent with the XRD data showing hematite in both samples. The platy hematite needles in the Milos BIF-type rocks are morphologically, and by size, comparable to hematite needles reported in the ~2.5 Ga Kuruman BIFs (Sun et al., 2015).

Unlike the Fe-rich bands, volcaniclasts in the Si-rich bands are much smaller in size, occurring mainly as fine-grained (Supplementary Fig. 8-11), signifying predominant precipitation during periods of weakened hydrothermal activity. The SiO_2 matrix in both the MFIF and NFIF are fine-grained, occurring mainly as amorphous opal in the NFIF (Figs 10B & 12A-B), whereas in the MFIF it is mainly present as crystalline quartz (Fig. 12C-D). Relative concentrations of Al, K and Ti in the samples are generally low, with bulk-measured concentrations in both the Si-/Fe-rich bands, together with the SiO_2 and Fe_2O_3 content, covarying with continental crust concentrations (Fig. 13A). Mn impregnation of the MFIF, preserved in the form of replacement layers mostly identified as cryptomelane [$K(Mn^{4+},Mn^{2+})_8O_{16}$) (Table 1), is below detection in the NFIF. Rare hausmannite ($Mn^{2+}Mn^{3+}{}_2O_4$) was detected in a few cases in the MFIF (Fig. 10D).

Ernest Chi Fru 29/3/2018 10:57
Deleted: strongly

3.3.3 Hydrothermal versus continental weathering

Trends of major elements from which CIA indices were calculated (Fig. 13B), covary with those of the continental crust (Fig. 13A). Continental crust averages, refer to the zone from the upper continental crust to the boundary with the mantle (Rudnick & Gao, 2003). The calculated CIA indices average 52 with one outlier at 22 (Fig. 13B). No distinct relationship could be established between the CIA indices and the respective IFs or between the distinct alternating Si- and Fe-rich bands (Fig. 13).

Highly weathered clay minerals resulting from the chemical decomposition of volcanic rocks, e.g., kaolinite representing maximum CIA values of 100 or 75-90 for illite, are absent in the analyzed materials. The absence of carbonates in the rocks strengthened the CIA indices, since CIA indices are expected to be lower when Ca carbonates are present (Bahlburg and Dobrzinski, 2011). TiO_2 content, a detrital proxy, is mostly constant and covaries with the CIA values (Fig. 13B), suggesting little variability and limited continental weathering input. A fairly strong negative linear correlation was found between SiO_2 and Fe_2O_3 values normalized to TiO_2 (inset, Fig. 13B).

3.3.4 Redox reconstruction

Redox reconstruction by sequential iron extraction (Poulton and Canfield, 2005, 2011; Guilbaud et al., 2015; Sperling et al., 2015) is consistent with deposition of both the MFIF and NFIF facies beneath an anoxic, ferruginous bottom water body (Fig. 13C-D). The shale-normalized REE values ($REE_{(SN)}$) for both the MFIF and NFIF are consistent with previous reports (Chi Fru et al., 2013, 2015), showing patterns typical of marine sedimentary environments affected by hydrothermal activity throughout Earth's history (e.g., Planavsky et al., 2010). There is a notable absence of significant negative $Ce_{(SN)}$ anomalies for both the MFIF and NFIF (Fig. 14A-B). These observations are statistically corroborated by true Ce anomalies. Further, the Eu/Eu* anomaly averages for the MFIF and NFIF and the distinct Fe-/Si-rich bands, suggest a ~2× higher Eu/Eu* signal for the Si-rich bands relative to the Fe-rich bands and between the MFIF and NFIF deposits (Fig. 14C). Average Pr and Yb shale-normalized ratios (Pr/Yb*), a light vs. heavy REE enrichment proxy (Planavsky et al., 2010), indicate similar depleted levels of light and heavy REE in

both the NFIF and MFIF, as well as in the Fe- and Si-rich bands (Fig. 14C). This independent verification of the anoxic depositional conditions using the sequential Fe proxy, suggests the NASC normalization protocol effectively captures the redox depositional conditions of the Milos IF.

3.4 Lipid biomarker distribution and chemotaxonomy

Bulk $\delta^{13}C_{org}$ averaged −25.4‰ (SD:±0.22); −25.2‰ (±0.26) for NFIF Fe-/Si-rich bands and −25.6‰ (SD:±0.12) for bulk MFIF, respectively (Table 2). A fractionation effect between the alternating Fe-/Si-rich layers ($\Delta^{13}C_{\text{Fe-rich NFIF-Si-rich NFIF}}$) is estimated to be ~0.23‰ (SD±0.036), while $\Delta^{13}C_{\text{Fe-rich NFIF-MFIF}}$ and $\Delta^{13}C_{\text{Si-rich NFIF-bulk MFIF}}$, is 0.13‰ (SD:±0.11) and 0.36‰ (SD:±0.14), respectively. These differences are small and within the margin of error of analysis, suggesting no strong distinction in $\delta^{13}C_{org}$ preserved in the different IFs and their various facies. They are interpreted to mean similar carbon fixation processes operated during intervals of predominant Si and Fe(III)(oxyhydr)oxides deposition in both IFs. Attempts to discriminate between these environments by lipid biomarker analysis revealed mainly C_{16}-C_{19} fatty acid methyl esters (FAME) in the Fe-rich NFIF bands and in bulk MFIF, while the Si-rich NFIF bands contain mainly C_{12}-C_{21} FAMEs, suggesting either selective preservation (lipid recovery was lower in the Fe-rich MFIF bands) or shifts to different potential biological populations during the deposition of the different layers. Preserved lipids discriminate against typical microbial lipid biomarkers like hopanoids, while C3 plant FAME are detected in all studied materials (Fig. 15). However, the anaerobic bacteria indicator, $10MeC_{16:0}$ FAME, was identified in a few bands.

4 Discussion

556 **4.1 Sedimentological processes**

557 The three sub-basin division of the CVSB is consistent with previous proposals
558 suggesting that sedimentation within the CVSB was characterized by active
559 synvolcanic rifting which must have been important in shaping basin topography and
560 the creation of sub-basin architecture (Papanikolaou et al., 1990; Stewart and McPhie,
561 2006; Liakopoulos et al., 2001; Papavassiliou et al., 2017). Moreover, this tectonic
562 regime would suggest that the location(s) of volcanism were continually changing
563 relative to the two stratigraphic sections, which themselves were also being affected,
564 i.e. changes in depositional water depth and sedimentation style or and/or that local
565 submarine or subaerial topographic highs impeded the lateral continuity of
566 sedimentary units (Stewart and McPhie, 2006). Chi Fru et al. (2015) have suggested
567 there is an upward deepening of the overall depositional setting recorded in the "Little
568 Vani" section, consistent with rifting during CVSB infilling time.

569 The CVSB floored by dacitic/andesitic lava domes and overlain by
570 vocaniclastic infill, dates back to Upper Pliocene-Lower Pleistocene. A complex
571 mosaic of lithologically diverse sedimentary units (blocks), confined by neotectonic
572 marginal faults, characterizes the CVSB (Fig. 2). The most pronounced of these faults
573 being the NW-trending Vromolimni-Kondaros fault (Papanikolaou et al., 1990) that
574 has been proposed as the trigger of the hydrothermal activity that deposited Mn ore in
575 the CVSB (Papanikolaou et al., 1990; Liakopoulos et al., 2001; Alfieris et al., 2013;
576 Papavassiliou et al., 2017). The stratigraphically tight coupling between Mn and Fe
577 deposition, linked by Fe oxide minerals in feeder-veins, and positive Eu anomalies
578 (Fig. 14) indicating vent-sourced Fe (Maynard, 2010), associate Fe mineralization to
579 fault-triggered hydrothermalism in the CVSB. This is consistent with models of
580 geothermal fluid circulation along fault lines as conduits for the Mn-rich fluids that

581 formed the Milos Mn ore deposit (Hein et al., 2000; Liakopoulos et al., 2001; Glasby
582 et al., 2005; Kilias, 2011; Papavassiliou et al., 2017). More importantly, the overall
583 complex neotectonic structure of the CVSB (Papanikolaou et al., 1990) would explain
584 the creation of restricted basins, with sedimentological, lithological and geothermal
585 conditions that enabled the development of unique biogeochemical circumstances in
586 which the NFIF and MFIF formed.

587 The presence of the three depositional basins is supported by the fact that the
588 sequence lithologies in each fault-bound unit are characterized exclusively by
589 occurrences of specific and variably thick stratigraphic packages that tend to be
590 absent in others. For example, the MFIF occurs restricted to basin 1 and the NFIF to
591 Basin 3. Basin 2 is further distinguished by 35-50 m thick interbedded ore-grade Mn-
592 mineralized and glauconitic sandstones/sandy tuffs, much less developed in Basins 1
593 and 3 (Fig. 2). The presence or absence of a stratigraphic sequence, together with its
594 thickness variation, are interpreted as a result of local syntectonic sediment formation
595 conditions in each basin as a result of block tectonic movements along fault lines
596 (Papanikolaou et al., 1990). It may also be attributed to unique basin scale water
597 column redox conditions (e.g. Bekker et al., 2010, and references therein), post-
598 depositional erosion and changing sea level stand (Cattaneo & Steel, 2000).

599 The lack of hydrothermal feeder veins or seafloor exhalative structures (i.e.,
600 chimneys) in the MFIF and NFIF lithologies, suggests that hydrothermal Fe(II) was
601 delivered by diffuse flow and that the Milos-IF formed on the seafloor.
602 Further, mineralisation of the MFIF is suggested to have occurred during two major
603 hydrothermal venting stages. The first produced the MFIF and the second
604 contaminated it with cryptomelane. Cryptomelane in the MFIF is therefore not a
605 replacement product of primary Mn oxides formed during the deposition of the MFIF,

because the anoxia prevailing in Basin 1 at the time (Figs 2 & 13C) would have precluded the precipitation of Mn oxide minerals, hinting that a second phase hydrothermal fluid emission rich in dissolved Mn, directly precipitated cryptomelane from solution as a secondary mineral relative to the primary Fe(III)(oxyhydr)oxides in the MFIF. This occurred during an episode when the MFIF deposit must have been exposed to oxygenated fluids, most likely through mixing with seawater at depth, indicated by the abundance of cryptomelane at the base of the MFIF. Our model for cryptomelane precipitation in the MFIF is therefore different from the one suggesting diagenetic transformation of primary Mn ores at Milos (Hein et al., 2001; Liakopoulous et al., 2001; Papavassiliou et al. 2017).

Geomorphological/chemical reconfiguration orchestrated the deposition of the NFIF in a deeper, small-restricted basin (Fig. 2). The deepening of Basin 3 is reflected in the underlying graded conglomerate bed that exhibits an upward fining trend, followed by transition into the fine-grain NFIF. The conglomerate bed may represent rapid deposition during a high-energy event, i.e. storm or mass flow, whereas the upward fining in the bed is better explained by the depositional mechanism losing energy through time. These high-energy conditions must have ceased during the deposition of the overlying NFIF, where we interpret that increased abundance of finely laminated IF and decreased evidence of storm and/or mass flow reworking reflects deepening conditions. The hypothesized deepening of Basin 3 is consistent with the interpretation that active rifting was an important mechanism in the formation of the CVSB (Papanikolaou et al., 1990).

Ernest Chi Fru 29/3/2018 11:04
Deleted: apparently

4.2 Formation Mechanism of The Milos BIFs

4.2.1 Paragenetic sequence

It is stressed that the previously generalized model proposed for biological deposition of the Milos IF, refers exclusively to parts of what is now designated as MFIF (Chi Fru et al., 2013). The NFIF is banded, but does not display the typical microfossils seen in the MFIF, where diffused microbanding apparently relates to the distribution of microbial mats in thin sections (Chi Fru et al., 2013, 2015). The distinction of microcrystalline quartz and amorphous silica phases in the MFIF and NFIF, respectively, together with nano-crystalline hematite particles, suggests a primary amorphous silica origin in both deposits, diagenetically transformed to quartz in the MFIF. The difference in silica crystallinity between the IFs is concurrent with the older age predicted for the MFIF relative to the NFIF, from reconstructed sequence stratigraphy (Fig. 2). Hematite in BIFs is generally interpreted, based on thermodynamic stability, to be a transformation product of various primary Fe(III) minerals, with ferrihydrite often proposed as the primary water column precipitate (Glasby and Schulz, 1999; Bekker et al., 2010; Johnson et al., 2008; Percoits et al., 2009). It is thought that acidic pH yields mainly goethite while hematite is produced at circumneutral pH (Schwertmann and Murad, 2007). The notable absence of diagenetic magnetite and Fe carbonates (siderite and ankerite), point to negligible coupling of primary Fe(III) oxyhydroxides reduction to organic matter oxidation by the dissimilatory iron-reducing bacteria during burial diagenesis (Johnson et al., 2008). Minor occurrence of iron-silicate phases (Chi Fru et al., 2015) indicates an origin of the hematite precursor in seawater independent of the iron silicate proposed in some cases (Fischer and Knoll, 2009; Rasmussen et al., 2013, 2014). The up to 50 wt% Fe content recorded in the Fe-rich bands, indicate that large amounts of dissolved Fe(II) was intermittently sourced and deposited as primary Fe(III) minerals, through various oxidative processes in the depositional basin.

Ernest Chi Fru 29/3/2018 10:58
Deleted: strongly

Importantly, the CIA analysis does not support mass weathering and mineralization of terrestrial Fe and Si, in agreement with the absence of rivers draining into the CVSB (Chi Fru et al., 2013). The specific identification of plant biolipids would at face value imply post-depositional contamination. However, samples were sawn to remove exposed layers and only the laminated bands for the NFIF were analyzed. Modern sediments from Spathi bay, located Southeast of Milos Island where hydrothermal activity is presently ensuing at 12.5 m below sea level, revealed similar plant lipids as recorded in the Quaternary IF (Fig. 15G). Post-depositional contamination with terrestrial plant lipids is therefore ruled out for the idea that recalcitrant plant biomass probably entered the sediments via seawater entrainment at the time of deposition (see Naden et al., 2005). This finding necessitates the careful interpretation of bulk $\delta^{13}C_{org}$ values obtained from both the modern and ancient Milos sediments, involving in situ and ex situ biological contributions to $^{13}C_{org}$ fractionation by various known carbon fixation pathways (Preuß et al., 1989; Berg et al., 2010).

4.2.2 Tectono-sedimentary processes and band formation

Fluctuation in hydrothermal activity is proposed to account for the banding in the NFIF (Fig. 16), under redox depositional conditions inferred to be mainly reducing for both investigated IFs, consistent with previous reports (Chi Fru et al., 2013, 2015). Positive Eu anomalies indicate a hydrothermal origin for all but one of the sample suite (Fig. 14A). However, statistically calculated Eu/Eu* anomalies ($Eu_{(SN)}/(0.66Sm_{(SN)} + 0.33Tb_{(SN)})$) to correct for differences in Gd anomalies commonly encountered in seawater (Planavsky et al., 2010) are in the range of 0.1-0.58, averaging 0.42. The lack of statistically significant true negative Ce anomalies (Fig.

683 14B) supported by sequential Fe redox reconstruction (Fig. 3C-D; Planavsky et al.,
684 2010; Poulton and Canfield, 2005, 2011; Guilbaud et al., 2015; Sperling et al. 2015),
685 indicate a reducing depositional environment for both The MFIF and the NFIF.

686 CIA analyses traditionally provide relative information on contributions from
687 chemical weathering to sediment deposition, linked to operative hydrological and
688 climatological patterns on land. This information is often gleaned from ancient and
689 modern soils and from reworked siliclastic deposits in marine basins (Maynard, 1993;
690 Bahlburg & Dobrzinski, 2011). The calculated CIA values, however, are closer to the
691 range obtained for unweathered and or only minimally weathered volcanic rocks (e.g.,
692 Nesbitt & Young, 1982; Bahlburg & Dobrzinski, 2011), thus pointing to a
693 predominantly volcanic and/or hydrothermal provenance for the clastic sedimentary
694 materials in the IFs.

695 It has been suggested that the release of reduced submarine hydrothermal fluids
696 contributed towards maintaining water column anoxia during the deposition of
697 Precambrian BIFs (Bekker et al., 2010). The calculated Eu anomalies (Fig. 14) and
698 petrographic data showing volcaniclastic detritus (i.e., K-feldspar, sanidine, tridymite,
699 cristobalite) as key rock components are in agreement with a submarine hydrothermal
700 source for the investigated IFs. The coarse volcaniclastic detritus embedded in the Fe-
701 rich bands compared to the finer particles in the Si-rich layers, highlights rapid
702 oxidation of Fe(II) that coincided with periodic cycles of hydrothermal/volcanic
703 discharge of new materials into the water column. However, the fine-grained nature
704 of both the MFIF and NFIF deposits suggests that deposition likely occurred away
705 from where such activity was occurring or that volcanic/hydrothermal discharge of Fe
706 and Si was non-eruptive and disruptive. The Fe-rich bands repetitively revealed
707 hematite grains cementing the denser volcaniclastic fragments that gradually diminish

upwards into a zone of fine-grained hematite before transitioning into Si-rich bands consisting mainly of finer volcaniclastic detritus. These observations provide three valuable interpretational considerations for proposing a model for the formation of the alternating Si and Fe-rich bands.

1. The Si and Fe oxides-rich bands are primary precipitates formed in the water column, by a process in which the precipitation of amorphous Si occurred during quiescent non-volcanic intervals, with the oxidation and precipitation of reduced Fe intermittently introduced into the water column by volcanic/hydrothermal activity to form the Fe oxides.
2. The repetitive zonation of distinct particle sizes, suggests density gradient sedimentation that requires a water column-like environment, rather than diagenetic alteration of pre-formed sediments by hydrothermal fluids.
3. The reducing depositional conditions do not support sediment diagenesis as an alternative model for explaining the origin of the Milos IF. This is because the oxidation of ferrous Fe supplied in reduced hydrothermal fluids, must interact with a sizeable pool of oxygen, enabling microaerophilic bacteria oxidation of ferrous iron to Fe(III)(oxyhydr)oxides (Johnson et al., 2008; Chi Fru et al., 2012). Otherwise, light-controlled photoferrotrophy, an extremely rare sediment characteristic, precipitates Fe oxides in the absence of oxygen in sunlight environments (Weber et al., 2006).

4.2.3 Biological involvement

Hematite precipitation in the MFIF on microbial filaments (Chi Fru et al., 2013) was previously used to propose a generalized basin-scale mechanism for the deposition of Fe-rich rocks in Cape Vani. However, such filaments are absent in the NFIF, while

733 pure hematite grains are tightly bound to relics of an organic matter signal carrying a
734 maximum $\delta^{13}C_{org}$ signature of -25‰ (Table 2). Similar processes are recorded in
735 modern marine sediments where interactions between Fe and free organic matter has
736 been reported to enable the preservation up to 21.5wt% of total organic carbon over
737 geological time scales (Lalonde et al., 2012). Moreover, Fe generally traps and
738 preserves organic matter at redox interfaces (Riedel et al., 2013)**.** The data appear to
739 suggest that the mechanism of Fe(III) (oxyhydr)oxide precipitation and preservation
740 varied between the two IFs. The photoferrotrophic-like filamentous fossils reported in
741 the MFIF (Chi Fru et al., 2013), are absent in the NFIF. This does not, however, rule
742 out the potential role of microbial involvement in Fe(II) oxidation, as diverse
743 microbial taxa carry out this process, several of which are non-filamentous (Chi Fru et
744 al., 2012). However, our data is insufficient to enable clear quantification of the levels
745 of abiotic vs. biotic contribution to Fe(II) oxidation in the NFIF. Nevertheless, the
746 inferred predominantly anoxic depositional conditions as explained above, together
747 with the identification of anaerobic bacteria biomarkers in the laminated bands,
748 intuitively favor significant contribution of anaerobic biological Fe(II) oxidation in
749 the precipitation of primary Fe(III)(oxyhydr)oxides in the NFIF. See Weber et al.,
750 2006, for a review of potential biological pathways to anaerobic Fe(II) oxidation.
751 Briefly, anaerobic microbial Fe(II) oxidation can proceed via nitrate reduction
752 and by photoferrotrophy to deposit Fe(III)(oxyhydr)oxides. These mechanisms have
753 been linked to microbial contribution to BIF formation (Weber et al., 2006; Kappler et
754 al., 2005) and also for the MFIF (Chi Fru et al., 2013). However, it is also possible
755 that microaerophilic neutrophilic Fe(II)-oxidizing bacteria likely played an important
756 role, assuming a depositional setting analogous to the Santorini caldera and Kolumbo
757 shallow submarine volcanoes, where such low-O_2-dependent microbial Fe(II)

758 oxidation has been identified to actively precipitate Fe(III) (oxyhydr)oxides (Kilias et
759 al., 2013b; Camilli et al., 2015). It appears that in the MFIF, precipitating
760 Fe(III)(oxyhydr)oxide minerals were bound and preserved free of organic carbon or
761 that such organic carbon was diagenetically degraded. As was previously shown,
762 Fe(III)(oxyhydr)oxides completely replaced the organic content of the filamentous
763 microfossils in the MFIF (Chi Fru et al., 2013).

764 The $10MeC_{16:0}$ FAME identified in the rocks has been reported in anaerobic
765 organisms coupling nitrite reduction to methane oxidation (Kool et al., 2012), in
766 sulfate and iron-reducing bacterial species such as Desulfobacter, Desulfobacula
767 (Bühring et al., 2005; Dowling et al., 1986; Taylor and Parkes, 1983), Geobacter,
768 Marinobacter and the marine denitrifier, Pseudomonas nautical (Kool et al., 2006;
769 Bühring et al., 2005; Dowling et al., 1986). It had previously been proposed that post-
770 depositional denitrification was a potential pathway for early organic matter removal,
771 justified by the low rock organic carbon and nitrogen content in the Milos BIF-type
772 rocks (Chi Fru et al., 2013, 2015; Table 2). Equally, the detected $10MeC_{16:0}$ FAME
773 has also been found in anaerobic oxidation of methane (AOM) communities (Alain et
774 al., 2006; Blumenberg et al., 2004), originating from sulfate reducing bacteria.
775 However, bulk sediment $\delta^{13}C_{org}$ of −20‰ does not reflect AOM activity that is
776 expected to produce bulk $\delta^{13}C_{org}$ values that are ≤−30‰. Low $10MeC_{16:0}$ FAME
777 concentrations frustrated attempts at acquiring its compound specific isotopic
778 signature to enable further biomolecular level reconstruction of active microbial
779 metabolisms to explain Fe deposition mechanisms.

780 It is nevertheless puzzling why potential microbial biomarkers typical of marine
781 or hydrothermal vent environments are hardly preserved in the rocks, given that
782 microfossil evidence indicates a vast community of diverse prokaryotic assemblages

783 in the adjacent MFIF (Chi Fru et al., 2013, 2015). Moreover, sediments of the modern
784 Milos hydrothermal system and elsewhere on the HVA, are ubiquitously colonized by
785 microbial life, characterized by the marked large-scale absence or low abundance of
786 higher life forms, including plants (Kilias et al., 2013b; Camilli et al., 2015; Oulas et
787 al., 2015). One possibility could be the discriminatory preservation of lipids related to
788 their selectivity and reactivity towards Fe(III)(oxyhydr)oxides and clays or different
789 pathways to diagenetic degradation (e.g., Canuel & Martens, 1996; Lü et al., 2010;
790 Riedel et al., 2013). As noted, the carbonaceous materials in the BIF-type NFIF rocks
791 occur in tight association with hematite.

792 Importantly, prokaryotic biomarkers are suggested to poorly preserve in these
793 young BIF analogs. This raises the possibility that this may provide an important
794 explanation for why lipid biomarkers are yet to be extracted from Precambrian BIFs.
795 Moreover, the data are compatible with the low C_{org} recorded in BIFs of all ages,
796 suggesting that the low C_{org} abundance may not be due to metamorphism as often
797 proposed (Bekker et al., 2010) or to C_{org} oxidation by dissimilatory iron reducing
798 bacteria to form ^{13}C-depleted siderite and ankerite during diagenesis (Johnson et al.,
799 2008; Bekker et al., 2010). The Milos BIF-type rocks are unmetamorphosed and lack
800 iron carbonate, yet have vanishingly low C_{org} levels similar to the ancient
801 metamorphosed BIFs. However, an alternative possibility is that the iron oxides may
802 have been reduced through biological oxidation of organic carbon, but carbonate
803 saturation was not reached (Smith et al., 2013).

804

805 **4.2.4 Mn layers and the deposition of the Si-Fe-rich facies**

806 Cryptomelane [K(Mn4+,Mn2+)8O16], which commonly occurs in oxidized Mn
807 deposits resulting from mineral replacement and as open space fillings (Papavassiliou

Ernest C 29/3/2018 12:59
Deleted: analogue

et al., 2016), is also common in the MFIF. This supports the idea of post-depositional impregnation of the base of the MFIF by Mn-rich fluids. Microscopic analysis supports the epigenetic origin of the Mn in the MFIF by revealing Mn oxides growing along fractures, impregnating and replacing Fe minerals (Fig. 4B-F). The macroscopically evident thinning out to disappearance of such Mn-rich horizons up the MFIF, coupled by their development along microfractures emphasizes this epigenetic origin. Mn is not a common feature of the NFIF, even though it sits on top of a thin sandstone layer that is highly mineralized with Mn, locally forming the cap of the main Mn ore at Cape Vani. The generally accepted view is that Mn-rich hydrothermal fluids rose and mineralized the Cape Vani sandstones (Hein et al., 2000; Liakopoulos et al., 2001; Glasby et al., 2005). Based on the stratigraphic location of the MFIF, which pre-dates the Mn-rich sandstones, it is proposed that impregnation of the MFIF by Mn was coeval with large-scale Mn ore mineralization of the Cape Vani sandstones, implying the entire basin was likely oxygenated at the time. The lack of Ce anomalies, confirmed by the sequential Fe extraction proxy data, suggests that both the MFIF and the NFIF formed in anoxic settings. Similar data for the Mn oxides have suggested formation in oxic settings (Glasby et al., 2005; Chi Fru et al., 2015). This implies that Mn epigenetically replaced the MFIF, either because the basin was tectonically uplifted into a high–energy oxygenated shallow water setting or that sea level dropped, leading to partial metasomatism of the base of MFIF, when oxygenated seawater mixed with reduced hydrothermal fluids and precipitated Mn. The lack of significant Ce anomalies in the dataset, combined with the inferred deepening of basin 3 and the anoxic depositional conditions suggested by the sequential iron redox proxy, further indicate that for the final deposition of the NFIF, an eventual deepening event must have been triggered, resulting in deoxygenation of parts of the CVSB.

834 All of this is feasible with the three-basin-fault-bounded hypothesis as a
835 requirement for movement along fault lines in response to temporal tectonic
836 activation. The upward sequence transition from the Mn-rich sandstone facies,
837 through the pebbly conglomerate and the final termination in the overlying mud-
838 grained NFIF (Fig. 8B), reflect sedimentary features formed during multiple changes
839 in seawater levels (Cattaneo & Steel, 2000).
840 Uplifting is suggested by potential weathering of the NFIF to form the
841 ferruginous duricrust cap. Comparable ferruginous layers on Precambrian BIFs are
842 linked to pervasive subaerial chemical weathering, via the dissolution of the silica-
843 rich layers and precipitation of relatively stable Fe oxides in the spaces between more
844 resistant hematite crystals (e.g., Dorr, 1964; Shuster et al., 2012; Levett et al., 2016).
845 This collective evidence supports the existence of a geodynamic tectonic system
846 capable of producing shallow oxic to deeper anoxic basin conditions at different times
847 that would explain the existence of Mn and Fe oxide layers within the same
848 sedimentary sequence. For example, it is common knowledge that both Fe and Mn
849 oxides will precipitate in the presence of oxygen (Roy, 1997, 2006), with kinetic rates
850 usually being faster for the oxidation of reduced Fe than reduced Mn. In the Fe(II)-
851 rich conditions that prevail in anoxic settings, abiotic reactions between Fe(II) and Mn
852 oxides, produce Fe(III) leading to the dissolution of the Mn oxides to form reduced
853 Mn, implying Mn oxides should not accumulate (Dieke, 1985). Moreover, under these
854 conditions, biological precipitation of Fe(III) can occur rapidly, leaving dissolved Mn
855 in solution to be deposited when oxygen becomes available. Given that the
856 hydrothermal fluids of the Hellenic Volcanic Arc are commonly enriched in both
857 reduced Fe and Mn, the deposition of the MFIF and NFIF therefore implies there was
858 an existing mechanism that enabled the kinetic discrimination and deposition of the

oxides of Fe and Mn into separate settings, most likely dependent on prevailing redox conditions. The accumulation of the ferruginous duricrust layer, overprinted by redox sensitive Mn-nodules, above the NFIF indicates a new shallowing event might have terminated the formation of the NFIF.

4.2.5 Modern analogs on the HVA

Ernest C 29/3/2018 12:59
Deleted: analogue

Mechanistic explanation for the development of potential stratified waters and reducing conditions during the deposition of the Milos BIF is problematic. However, evidence is available from present shallow submarine hydrothermal analogs in the central part of the HVA, to which the CVSB belongs. These include:

Ernest C 29/3/2018 12:59
Deleted: analogue

(1) The crater floor of the Kolumbo shallow-submarine volcano (~600×1200 m), which rises from 504 to 18 m below sea level, near Santorini (Sigurdsson et al., 2006; Kilias et al., 2013b).

(2) The N part of Santorini's submerged caldera walls, which rises from 390 m below sea level to over 300 m above sea level (Druitt et al., 1999; Friedrich et al., 2006; Nomikou et al., 2013; Camilli et al., 2015).

(3) The coastal embayments at the Kameni emergent volcanic islands in the centre of the Santorini caldera (Hanert, 2002; Nomikou et al., 2014; Robbins et al., 2016).

The benthic waters within Kolumbo's crater potentially sustain O_2 depleted conditions via stable CO_2-induced water column densification, and accumulation of acidic water (pH ~5), extending ~10 m above the CO_2 venting crater floor (Kilias et al., 2013b). This phenomenon is believed to lead not only to obstruction of vertical mixing of bottom acidic water, but also to O_2 deprivation by precluding efficient transfer of oxygenated surface seawater into the deeper crater layer. In addition,

886 diffuse CO_2 degassing is believed to be linked to the formation of Fe microbial mats
887 and amorphous Fe(III) oxyhydroxides on the entire Kolumbo crater floor (Kilias et
888 al., 2013b) and on the shores of Milos Island (Callac et al., 2017). Prerequisites for
889 the O_2-depleted conditions to happen are the closed geometry of the Kolumbo crater
890 and the virtually pure CO_2 composition of the released hydrothermal vent fluids that
891 produce O_2 stratification along a stable CO_2-pH gradient.

892 A similar scenario is reported for the Santorini caldera, where large (~5 m
893 diameter) CO_2-rich, acidic (pH, ~5.93) hydrothermal seafloor pools and flow
894 channels, develop within m-thick microbial Fe-mats on the seafloor slope at 250-230
895 m below sea level. Persistent hypoxia exists in these pools, representing concentrated
896 seafloor CO_2 accumulation centers generated by hydrothermal venting (Camilli et al.,
897 2015). Here, the dissolved O_2 content (~80 μM or less) in the pools is ~40 % depleted
898 relative to the surrounding ambient seawater (Camilli et al., 2015). These hypoxic
899 conditions are comparable to or even lower than those measured in the CO_2-rich
900 oxygen minimum zones of coastal oceans, relative to seawater existing in equilibrium
901 with atmospheric pO_2 and pCO_2 pressures (Paulmier et al., 2008, 2011; Franco et al.,
902 2014). These conditions enable strong redox stratification of the pool waters, in which
903 unique Si- and Fe-rich microbial mats are associated with amorphous opal and
904 Fe(III)(oxyhydro)xides (Camilli et al., 2015). Importantly, the Fe microbial mats in
905 these CO_2-rich hypoxic pools are affiliated with specific microaerophilic Fe(II)-
906 oxidizing bacteria that accumulate Fe(III) oxyhydroxides (Camilli et al., 2015; Oulas
907 et al., 2015). These Fe bacteria are implicated in the deposition of the Precambrian
908 BIFs (Konhasuer et al., 2002; Planavsky et al., 2009; Bekker et al., 2010).

909 Hypoxia is also associated with the water column of the Fe(III)-rich coastal
910 embayments and their hydrothermal vents (≤1.0 m water depth), Kameni islands

911 (Hanert, 2002; Robbins et al., 2016 and references therein). Venting fluids are warm
912 (20-40 ^{o}C), acidic to circumneutral (pH 5.5-6.9), enriched in CO_2, Fe and Si
913 (Georgalas & Liatsikas, 1936, Boström et al., 1990; Handley et al., 2010; Robbins et
914 al., 2016). Water column stratification is expressed as decreasing O_2 with depth that is
915 positively related to Fe(III)(oxyhydr)oxide density and microaerophilic Fe(II)-
916 oxidizing bacterial prevalence (Hanert, 2002). Robbins et al. (2016) found that
917 Fe(III)-rich suspended particulate material in these "Fe bays" may be associated with
918 anoxia, extending up to the air-seawater interface, near the hydrothermal vents
919 (Hanert, 2002). They consist of ferrihydrite, goethite and microaerophilic Fe(II)
920 oxidizers.

921 However, the biogeochemical occurrence of these phenomena within the
922 localized confines of the Santorini caldera and Kolumbo crater, may however be
923 difficult to achieve in ordinary shallow submarine hydrothermal settings, such as
924 those occurring on the coast of present day Milos. The same may be true for Tatum
925 Bay, where non-volcanic and unconfined diffuse hydrothermalism is widespread
926 (Dando et al., 1996; Pichler & Dix, 1996; Pichler & Veizer, 1999; Stüben et al., 1999;
927 Rancourt et al., 2001; Varnavas et al., 2005).

928 In the Kolumbo and Santorini hydrothermal fields, benthic pH averages 5.5 and
929 the deposition of carbonates is markedly absent (Kilias et al., 2013b, Camilli et al.,
930 2015; Robins et al., 2016). This conforms to observations in the MFIF and NFIF units
931 where carbonate mineralization is not detected, thereby suggesting a similar low pH
932 depositional environment for both the MFIF and NFIF. Ubiquitous
933 Fe(III)(oxyhydr)oxide precipitation and enriched Si content are prevalent in the CO_2-
934 rich-hypoxic shallow submarine Santorini caldera slope pools and the Kameni Fe-
935 embayments where sulfide precipitation is inhibited (Camilli et al., 2015), or

936 extremely rare (Robbins et al., 2016). Such sulfide-poor conditions are critical for the
937 formation of BIFs (Bekker et al., 2010).
938 A high Si-Fe(III)(oxyhydr)oxide content, absence of carbonate and sulfide
939 mineralization, coupled to a generally low S content have also been demonstrated for
940 the CVSB Fe formations (Chi Fru et al., 2013, 2015). This depositional situation is
941 different, for example, from the unconfined shallow submarine hydrothermal systems
942 in Tatum Bay and Bahia Concepcion Bahia Carlifornia Sur, Mexico, where authigenic
943 carbonate deposition is widespread (Canet et al., 2005; Pichler & Veizer, 1996, 2005).
944 Moreover, there is strong geological evidence that within volcanic crater
945 environments associated with high CO_2 emission, long-term water column redox
946 stratification is possible under these special conditions. Further evidence is found in
947 volcanic crater lakes (for example the shallow 205 m deep lake Nyos in Cameroon—
948 renowned as one of Earth's three CO_2 saturated volcanic lakes (Ozawa et al., 2016;
949 Kling et al., 2005). Here CO_2-induced water column stratification is associated with
950 bottom reducing conditions characterized by a low sulfate and high Fe bottom water
951 content relative to surface concentrations (Tiodjio et al., 2014).
952
953 **5 Concluding remarks**
954 This study shows the following new insights in light of what was previously known:
955 1. At least two distinct IFs (MFIF and NFIF) formed from hydrothermal mud,
956 within two localized sub-basins in the ~1 km-long CVSB, ~2.66-1.0 Myr ago,
957 controlled by local tectonism.
958 2. Local conditions of elevated and cyclic supply of ferrous Fe and dissolved Si,
959 accompanied by strict bottom water anoxic conditions in a localized reservoir
960 cutoff from the open ocean, can in principle allow the deposition of BIF-type

961 rocks in a modern marine setting. The rarity of these types of deposits
962 however suggests that such conditions are extremely difficult to attain under
963 the modern oxygen-rich atmosphere.
964 3. A working model that band formation may involve potential
965 Fe(III)(oxyhydr)oxide filling of sediment pores and fractures during
966 diagenesis, is not supported by the data. In addition to the lack of observation
967 of such phenomena, as demonstrated for replacive Mn mineralization,
968 calculated Ce and Eu anomalies, together with sequential iron extraction
969 analysis, are suggestive of anoxic depositional conditions likely induced by
970 the release of reduced hydrothermal/volcanic fluids into a cutoff sedimentary
971 basin.
972 4. The precipitation of Fe(III) and Mn oxides require oxygen. In the absence of
973 oxygen, Mn is not oxidized, while light and photoferrotrophy will oxidize
974 reduced Fe to Fe(III)(oxyhydr)oxides. Both light and photoferrotrophy are
975 however extremely rare characteristics of anoxic sediments, but a common
976 feature of anoxic Fe^{2+}-rich waters, where photoferrotrophy is widespread
977 (Weber et al., 2006). Collectively, these observations provide an important
978 feasible mechanism for the knife sharp separation of the Mn oxide-rich ores
979 in the CVSB that are also Fe(III)(oxyhydr)oxide-rich, from the highly
980 localized MFIF and NFIF deposits that are Fe(III)(oxyhydr)oxide-rich but Mn
981 oxide-poor.
982 5. The mechanism of formation of the MFIF and NFIF therefore most likely
983 involved exhalative release of reduced hydrothermal/volcanic fluids into a
984 restricted and deoxygenated seafloor water column where the oxidation of
985 reduced Fe to Fe(III)(oxyhydr)oxides occurred, most likely by the activity of

photoferrotrophs (Chi Fru et al., 2013). Microaerophilic oxidation of Fe(II) was likely critical, but that remains to be shown.

6. Episodic intensification of hydrothermal activity is identified as a main mechanism for the formation of the millimetric BIF bands, adding to the biological mechanism that was inferred from fossil records in the MFIF (Chi Fru et al., 2013, 2015).
7. Abiotic Si precipitation was much slower relative to Fe(III) precipitation, resulting in Fe-rich bands in the NFIF forming in association with large fragments of volcaniclast and the Si-rich bands with finer Si grains.
8. A combination of the above processes produced pulses of Si and Fe in the millimetric Si and Fe-rich bands in the NFIF.
9. The Milos rocks fulfill sedimentological, chemical and mineralogical characteristics that established them as potentially the youngest known BIFs; following the simplistic definition that BIFs are sedimentary rocks composed of alternating layers of Fe and Si containing at least 15% Fe.
10. Whether the rocks described here are analogs of Precambrian BIFs or not, and whether the proposed formation mechanisms match those that formed the ancient rocks, is opened to debate. However, there are many similarities to proposed Precambrian BIF depositional models (e.g. Klien, 2005; Beukes and Gutzmer, 2008; Smith et al., 2013; Bekker et al., 2010; Klein and Beukes, 1992). Importantly, the present study provides mechanisms by which rocks with alternating Fe and Si-rich bands can be formed in the modern ocean.

Data availability. Data can be accessed by request from any of the authors

Ernest Chi Fru 29/3/2018 11:04
Deleted: apparently

Ernest C 29/3/2018 12:59
Deleted: analogue

Author contributions. ECF, SK and MI designed the study. ECF, SK, KG and MI performed fieldwork. ECF, JER, KG, IM and QH performed research. ECF, SK, KG, MI, QH and JER interpreted data. ECF and SK wrote paper.

Competing interests. The authors declare that they have no conflict of interest.

Acknowledgments. Ariadne Argyraki, Nicole Posth, Nolwenn Callac and Eva Zygouri are acknowledged field assistance during sampling and for stimulating intellectual discussions. Special thanks to Christoffer Hemmingsson for contributing to the SEM and XRD analyses. Christophe Brosson is acknowledged for his work on sequential iron extraction. This work is funded by the European Research Council (ERC) Seventh Framework Program (FP7) grant No. 336092 and the Swedish Research Council grant No. 2012-4364.

References

Alain, K., Holler, T., Musat, F., Elvert, M., Treude, T., and Kruger M.; Microbiological investigation of methane- and hydrocarbon-discharging mud volcanoes in the Carpathian Mountains, Romania. Environ. Microbiol., 8, 574–590, 2006.

1037 Alfieris, D. and Voudouris, P.: Ore mineralogy of transitional submarine magnatic-
1038 hydrothermal deposits in W. Milos Island, Greece. Bul. Acad. Sci., 43, 1–6, 2005.
1039 Alfieris, D.; Geological, geochemical and mineralogical studies of shallow submarine
1040 epithermal mineralization in an emergent volcanic edifice, at Milos Island (western
1041 side), Greece. PhD thesis, Department Geowissenschaften der Universität
1042 Hamburg, 2006.
1043 Alfieris, D., Voudouris, P., and Spry, P.: Shallow submarine epithermal Pb–Zn–Cu–
1044 Au–Ag–Te mineralization on western Milos Island, Aegean Volcanic Arc, Greece:
1045 Mineralogical, geological and geochemical constraints. Ore Geol. Rev., 53, 159–
1046 180, 2013.
1047 Anand, R. R., Paine, M., and Smith, R.E.: Genesis, Classification and Atlas of
1048 Ferruginous Materials, Yilgarn Craton. CRC LEME Open File Report vol. 13,
1049 CSIRO Exploration and Mining, Perth, 2002.
1050 Bahlburg, H. and Dobrzinski, N.: A review of the Chemical Index of Alteration (CIA)
1051 and its application to the study of Neoproterozoic glacial deposits and climate
1052 transition. Geol. Soc. London Mem., 36, 81–92, 2011.
1053 Bau, M. and Dulski, P.: Distribution of yttrium and rare- earth elements in the Penge
1054 and Kuruman Iron-Formations, oxidative scavenging of cerium on hydrous Fe
1055 oxide, Transvaal Supergroup, South Africa. Precambrian Res., 79, 37–55, 1996.
1056 Berg, I.A., Kockelkorn, D., Ramos-Vera, W.H., Say, R.F., Zarzycki, J., Hügler, M.,
1057 Alber, B.E., and Fuchs, G.: Autotrophic carbon fixation in archaea. Nat. Rev.
1058 Microbiol., 8, 447–460, 2010.
1059 Bekker, A., Slack J.F., Planavsky, N., Krapež B., Hofmann, A., Konhauser, K.O., and
1060 Rouxel, O.J.: Iron formation: The sedimentary product of a complex interplay

among mantle, tectonic, oceanic, and biospheric processes. Econ. Geol., 105, 467–508, 2010.

Beukes, N.J., and Gutzmer, J.: Origin and Paleoenvironmental significance of major Iron Formations at the Archean-Paleoproterozoic boundary. Econ. Geol. 15, 5–47, 2008.

Beukes, N.J., Swindell, E.P.W., Wabo, H.: Manganese deposits of Africa, Episodes v. 39, 285–317, 2016.

Blumenberg, M., Seifert, R., Reitner, J., Pape, T., and Michaelis, W.: Membrane lipid patterns typify distinct anaerobic methanotrophic consortia. Proc. Natl. Acad. Sci. U.S.A., 101, 11111–11116, 2004.

Boström, K., Honnorez, J., Joensuu, O., and Rydell, H.: Chemistry of hydrothermal solutions in drill hole GPK-1, Palaea Kameni, Santorini, Greece. Proceedings of the third international congress, Santorini, Greece. 3, 257–260, 1990.

Bronn, H.G.: Ubersicht der Fossilen Uberreste in den tertiären subappeninischen Gebirgen. Italiens Tertiär-Gebilde und deren organische Einschlüsse. Heidelberg pp. XII + 176 + 1 pl, 1831.

Bouma, A.H.: Sedimentology of Some Flysch Deposits. Amsterdam, Elsevier, pp. 168, 1962.

Breitkreuz, C.: Spherulites and lithophysae—200 years of investigation on hightemperature crystallization domains in silica-rich volcanic rocks. Bull. Volcanol., 75, 1–16, 2013.

Bühring, S.I., Elvert, M., and Witte, U.: The microbial community structure of different permeable sandy sediments characterized by the investigation of bacterial fatty acids and fluorescence in situ hybridization. Environ. Microbiol., 7, 281–293, 2005.

1086 Callac, N., Posth, N.R., Rattray, J.E., Yamoah, K.K.Y., Wiech, A., Ivarsson, M.,
1087 Hemmingsson, C., Kilias, S.P., Argyraki, A., Broman, C., Skogby, H.,
1088 Smittenberg, R.H., and Chi Fru, E.: Modes of carbon fixation in an arsenic and
1089 CO_2-rich shallow hydrothermal ecosystem. Sci. Rep., 7, 14708,
1090 doi:10.1038/s41598-017-13910-2, 2017.
1091 Camilli, R., Noumikou P., Escartin, J., Ridao, P., Mallios, A., Kilias, S.P., Argyraki,
1092 A., and the Caldera Science Team: The Kallisti Limnes, carbon dioxide
1093 accumulating subsea pools. Sci. Rep., 5, 12152, doi:10.1038/srep12152, 2015.
1094 Canuel, E.A. and Marten, C.S.: Reactivity of recently deposited organic matter:
1095 Degradation of lipid compounds near the sediment-water interface. Geochim.
1096 Cosmo. Acta, 60, 1793–1806, 1996.
1097 Canet, C., Prol-Ledesma, R.M., Torres-Alvarado, I., Gilg, H.A., Villanueva, R.E., and
1098 Cruz, R.L.S.: Silica-carbonate stromatolites related to coastal hydrothennal venting
1099 in Bahia Concepcion, Baja California Sur, Mexico. Sed. Geol., 174, 97–113, 2005.
1100 Cattaneo, A. and Steel, R.J.: Transgressive deposits: a review of their variability.
1101 Earth Sci. Rev., 62, 187–228, 2003.
1102 Chi Fru, E., Piccinelli, P., and Fortin, D.: Insights into the global microbial
1103 community structure associated with iron oxyhydroxide minerals deposited in the
1104 aerobic biogeosphere. Geomicrobiol. J., 29, 587-610, 2012.
1105 Chi Fru, E., Ivarsson, M., Kilias, S.P., Bengtson, S., Belivanova, V., Marone, F.,
1106 Fortin, D., Broman, C., and Stampanoni, M.: Fossilized iron bacteria reveal a
1107 pathway to the origin banded iron formations. Nat. Comm., 4, 2050 DOI:
1108 10.1038/ncomms3050, 2013.

1109 Chi Fru, E., Ivarsson, M., Kilias, S.P., Frings, P.J., Hemmingsson, C., Broman, C.,
1110 Bengtson, S. and Chatzitheodoridis, E.: Biogenicity of an Early Quaternary iron
1111 formation, Milos Island, Greece. Geobiology, 13, 225–44, 2015.
1112 Dando, P.R., Hughes, J.A., Leahy, Y., Niven, S.J., Taylor, L.J. and Smith, C.: Gas
1113 venting rates from submarine hydrothermal areas around the island of Milos,
1114 Hellenic Volcanic Arc. Cont. Shelf Res., 15, 913–925, 1995.
1115 Dieke, P. Concentration of Mn and separation from Fe in sediments—I. Kinetics and
1116 stoichiometry of the reaction between birnessite and dissolved Fe(II) at 10°C.
1117 Geochim. Cosmo. Acta, 49, 1023–1033, 1985.
1118 Dorr, J.V.N.: Supergene iron ores of Minas Gerais, Brazil. Econ. Geol., 59, 1203,
1119 1964.
1120 Dowling, N.J. E., Widdel, F., and White, D.C.: Phospholipid ester-linked fatty-acid
1121 biomarkers of acetate-oxidizing sulfate-reducers and other sulfide-forming
1122 bacteria. J. Gen. Microbiol., 132, 1815–1825, 1986.
1123 Druitt, T. H. L., Edwards, R. M., Mellors, D. M., Pyle, R. S. J., Sparks, M., Lanphere,
1124 M. D., and Barreirio, B.; Santorini Volcano. Geol. Soc. Mem. London, 19, 165,
1125 1999.
1126 Fischer, W.W. and Knoll, A.H.: An iron shuttle for deepwater silica in Late Archean
1127 and early Paleoproterozoic iron formation. Geol. Soc. Am. Bull., 121, 222–235,
1128 2009.
1129 Franco, A.C., Hernández-Ayón, J.M, Beie,r E., Garçon, V., Maske, H., Paulmier, A.,
1130 Färber-Lorda, J., Castro, R., and Sosa-Ávalos, R.: Air-sea CO_2 fluxes above the
1131 stratified oxygen minimum zone in the coastal region off Mexico. J. Geophy. Res.,
1132 119, 2923–2937, 2014.

1133 Friedrich, W.L., Kromer, B., Friedrich, M., Heinemeier, J., Pfeiffer, T., and Talamo,
1134 S.: Santorini eruption radiocarbon dated to 1627-1600 BC. Science, 312, 548–548,
1135 2006.
1136 Fytikas, M., Innocenti, F., Kolios, N., Manetti, P., Mazzuoli, R., Poli, G., Rita, F., and
1137 Villari, L.: Volcanology and petrology of volcanic products from the island of
1138 Milos and Neighbouring islets. J. Vol. Geotherm. Res., 28, 297–317, 1986.
1139 Galan, L.D.P., Doval, M., La Iglesia, A., Soriano, J., and Chavez, L.: Occurrence of
1140 silica polymorphs nanocrystals in tuffaceous rocks, Province of the Mesa Central,
1141 Mexico, and their formation from subcritical Si-rich fluids. Am. Mineral., 98, 977–
1142 985, 2013.
1143 Georgalas, G., and Liatsikas, N.: Die Historische entwickelung des Dafni-Ausbruches
1144 1925-1926. In Santorin, Der Werdegand eines Inselvulkans und sein Ausbruch
1145 1925-1928, V. 2 (ed. Reck, H.). Verlag von Dietrich Reimer, Berlin, 1–96 pp,
1146 1936.
1147 Glasby, G.P. and Schulz, H.D.: Eh, pH diagrams for Mn, Fe, Co, Ni, Cu and As under
1148 seawater conditions: application of two new types of the Eh, pH diagrams to the
1149 study of specific problems in marine geochemistry. Aquatic Geochem., 5, 227–
1150 248, 1999.
1151 Glasby, G.P., Papavassiliou, C.T., Mitsis, J., and Valsami-Jones, E.: The Vani
1152 manganese deposit, Milos island, Greece: A fossil stratabound
1153 Mn−Ba−Pb−Zn−As−Sb−W-rich hydrothermal deposit. Develop. Volcanol., 7,
1154 255–291, 2005.
1155 Gromet, L.P., Dymek, R.F., Haskin, L.A., and Korotev, R.L.: The North American
1156 shale composit: Its compilation and major trace element characteristics. Geochim.
1157 Cosmo. Acta, 48, 2469–2482, 1984.

Gross, G.A.: A classification of iron-formation based on depositional Environments. Can. Min., 18, 215–222, 1980.

Guilbaud, R., Poulton, S.W., Butterfield, N.J., Zhu, M., and Shields-Zou, G.A.: A global transition to ferruginous conditions during the early Neoproterozoic. Nat. Geosci. 8:466–470, 2015.

Handley, K. M., Boothman, C., Mills, R. A., Pancost, R. D., and Lloyd, J. R.: Functional diversity of bacteria in a ferruginous hydrothermal sediment. ISME J., 4, 1193-1205, 2010.

Hanert, H. H.: Bacterial and chemical iron oxide deposition in a shallow bay on Palaea Kameni, Santorini, Greece: microscopy, electron probe microanalysis, and photometry of in situ experiments. Geomicrobiol. J., 19, 317–342, 2002.

Hein, J. R., Stamatakis, M. G., and Dowling, J. S.: Trace metal-rich Quaternary hydrothermal manganese oxide and barite deposit, Milos Island, Greece. Applied Earth Science: Trans. Inst. Min. Metal. Section B., 109, 67–76, 2000.

Horwell, C.J., le Blond, S., Michnowicz, S. A. K. and Cressey, G.: Cristobalite in a rhyolitic lava dome: evolution of ash hazard. Bull. Volcanol. 72, 249-253, 2010.

Ichihara, K. and Fukubayashi, Y.: Preparation of fatty acid methyl esters for gas-liquid chromatography. J. Lipid Res., 51, 635–40, 2010.

James, H. L.: Sedimentary facies of iron-formation. Econ. Geol., 49, 235−293, 1954.

Johnson, C. M., Beard, B. L., and Roden, E. E.: The iron isotope fingerprints of redox and biogeochemical cycling in modern and ancient Earth. Ann. Rev. Earth Plan. Sci., 36, 457–493, 2008.

Kappler, A., Pasquero, C., and Newman, D.K.: Deposition of banded iron formations by anoxygenic phototrophic Fe(II)-oxidizing bacteria. Geology, 33, 865–868, 2005.

1183 Kilias, S. P., Detsi, K., Godelitsas, A., Typas, M., Naden, J., and Marantos, Y.:
1184 Evidence of Mn-oxide biomineralization, Vani Mn deposit, Milos, Greece. In:
1185 Proceedings of the ninth biennial Meeting of the Society for Geology Applied to
1186 Mineral Deposits, Dublin, Ireland. Irish Assoc. Econ. Geol. 1069–1072 pp, 2007.
1187 Kilias, S. P.: Microbial mat-related structures in the Quaternary Cape Vani
1188 manganese-oxide (-barite) deposit, NW Milos island, Greece. Soc. Sed. Geol. Sp.
1189 Pub., 101, 97–110, 2011.
1190 Kilias, S. P., Chatzitheodoridis, E., and Lyon, I.: Molecular, chemical and
1191 morphological evidence for hematite biogenicity at the Quaternary Cape Vani Mn-
1192 (Ba-Fe) deposit, Milos, Greece. Bull. Geol. Soc., 47, 834-842, 2013a.
1193 Kilias, P. S., Nomikou, P., Papanikolaou, D., Polymenakou, P. N., Godelitsas, A.,
1194 Argyraki, A., Carey, S., Gamaletsos, P., Mertzimekis, T. J., Stathopoulou, E.,
1195 Goettlicher, J., Steininger, R., Betzelou, K., Livanos, I., Christakis, C., Bell, K. C.:
1196 and Scoullos, M. New insights into hydrothermal vent processes in the unique
1197 shallow-submarine arc-volcano, Kolumbo (Santorini), Greece. Sci. Rep., 3,
1198 doi:10.1038/srep02421, 2013b.
1199 Klein, C.: Some Precambrian banded iron-formations (BIFs) from around the world:
1200 Their age, geologic setting, mineralogy, metamorphism, geochemistry, and origins.
1201 Am. Min., 90, 1473–1499, 2005.
1202 Kling, G. W., Evans, W. C., Tanyileke, G., Kusakabe, M., Ohba, T., Yoshida, Y., and
1203 Hell, J. V.: Degassing Lakes Nyos and Monoun: Defusing certain disaster. Proc.
1204 Natl. Acad. Sci. U.S.A., 102, 14185–14190, 2005.
1205 Klein, C., and Beukes, N.J.: Time distribution, stratigraphy and sedimentologic
1206 setting, and geochemistry of Precambrian Iron Formation. In Schopf, J. W., and

Klein, C.: The Proterozoic Biosphere: A multidisciplinary study, 139 – 146. Cambridge University Press, New York, 1992.

Konhauser, K. O., Planavsky, N. J., Hardisty, D. S., Robbins, L. J., Warchola, T. J., Haugaard, R., Lalonde, S. V., Partin, C. A., Oonk, P .B. H., Tsikos, H., and Lyons, T.W.: Iron formations: A global record of Neoarchaean to Palaeoproterozoic environmental history. Earth Sci. Rev., 172, 140-177, 2017.

Krapež, B., Barley, M. E., Pickard, A .L.: Hydrothermal and resedimented origins of the precursor sediments to banded iron formations: Sedimentological evidence from the early Palaeoproterozoic Brockman Supersequence of Western Australia. Sedimentology, 50, 979-1011, 2003.

Lalonde, K., Mucci, A., Quellet, A. and Gélinas, Y.: Preservation of organic matter in sediments promoted by iron. Nature, 483, 198–200, 2012.

Levett, A., Gagen, E., Shuster, J., Rintoul, L., Tobin, M., Vongsvivut, J., Bambery, K., Vasconcelos, P., and Southam, G.: Evidence of biogeochemical processes in iron duricrust formation. J. South. Am. Earth Sci., 71, 131–142, 2016.

Li, W., Czaja, A. D., Van Kranendonk, M. J., Beard, B. L., Roden, E. E., Johnson, C. M.: An anoxic, Fe(II)-rich, U-poor ocean 3.46 billion years ago. Geochim. Cosmo. Acta, 120, 65-79, 2013.

Liakopoulos, A., Glasby, G. P., Papavassiliou, C. T. and Boulegue, J.: Nature and origin of the Vani manganese deposit, Milos, Greece: an overview. Ore Geol. Rev., 18, 181–209, 2001.

Lü, D., Song, Q., and Wang, X.: Decomposition of algal lipids in clay-enriched marine sediment under oxic and anoxic conditions. Chin. J. Oceanogr. Limnol., 28, 131–143, 2010.

1231 Marschik, R., Bauer, T., Hensler, A.-S., Skarpelis, N., and Hölzl, S. Isotope
1232 Geochemistry of the Pb-Zn-Ba(-Ag-Au) Mineralization at Triades-Galana, Milos
1233 Island, Greece. Res. Geol., 60, 335–347, 2010.
1234 Maynard, J. B.: Chemistry of modern soils as a guide to interpreting Precambrian
1235 Paleosols. J. Geol., 100, 279–289, 1993.
1236 Maynard, J. B.: The chemistry of manganese ores through time: a signal of increasing
1237 diversity of earth-surface environments. Econ. Geol., 105, 535–552, 2010.
1238 McLennan, S.B.: Rare earth elements in sedimentary rocks. Influence of provenance
1239 and sedimentary processes. In: B.R. Lipin and G.A. McKay (Editors),
1240 Geochemistry and Mineralogyof the Rare Earth Elements. Mineralogical Society
1241 of America, Washington, pp. 169-200, 1989.
1242 Miall, A. D. Lithofacies types and vertical profile models in braided river deposits.
1243 Can. Soc. Pet. Geol. Mem., 5, 597–604, 1978.
1244 Miall, A. D.: Architectural element analysis: a new method of facies analysis applied
1245 to fluvial deposits. Earth Sci. Rev., 22, 261e308, 1985.
1246 Morris, R. V., Vaniman, D. T., Blake, D. F., Gellert, R., Chipera, S. J., Rampe, E. B.,
1247 Ming, D. W., Morrison, S. M., Downs, R. T., Treiman, A. H., Yen, A. S.,
1248 Grotzinger, J. P., Achilles, C. N., Bristow, T. F., Crisp, J. A., Des Marais, D. J.,
1249 Farmer, J. D., Fendrich, K. V., Frydenvang, J., Gradd, T. G., Morookian, J-M.,
1250 Stolper, E. M. and Schwenzer, S. P.: Silicic volcanism on Mars evidenced by
1251 tridymite in high-SiO2 sedimentary rock at Gale crater. Proc. Natl. Acad. Sci.
1252 U.S.A., 113, 7071–7076, 2016.
1253 Mutti, E.: Turbidite Sandstones. Agip Spe. Pub., 275 pp, 1992.
1254 Nesbitt, H. W. and Young, G. M.: Early Proterozoic climates and plate motions
1255 inferred from major element chemistry of lutites. Nature, 199, 715–717, 1982.

1256 Nomikou, P., Papanikolaou, D., Alexandri, M., Sakellariou, D., and Rousakis, G.:
1257 Submarine volcanoes along the Aegean volcanic arc. Tectonophysics, 597–598,
1258 123–146, 2013.
1259 Nomikou, P., Parks, M. M., Papanikolaou, D., Pyle, D. M., Mather, T. A., Carey, S.,
1260 Watts, A. B., Paulatto, M., Kalnins, M.L., Livanos, I., and Bejelou, K.: The
1261 emergence and growth of a submarine volcano: The Kameni islands, Santorini
1262 (Greece). Geo. Res. J., 1, 8–18, 2014.
1263 Ozawa, A., Ueda, A., Fantong, W. Y., Anazawa, K., Yoshida, Y., Kusakabe, M.,
1264 Ohba, T., Tanyileke, G., and Hell, J.V. Rate of siderite precipitation in Lake Nyos,
1265 Cameroon. Geol. Soc. London Sp. Pub., 437, doi.org/10.1144/SP437.13, 2016.
1266 Papanikolaou, D., Lekkas, E., and Syskakis, D.: Tectonic analysis of the geothermal
1267 field of Milos Island. Bull. Geol. Soc. Greece, 24, 27–46, 1990.
1268 Papavassiliou, K., Voudouris, P., Kanellopoulos, C., Glasby, G., Alfieris, D., and
1269 Mitsis, I.: New geochemical and mineralogical constraints on the genesis of the
1270 Vani hydrothermal manganese deposit at NW Milos island, Greece: Comparison
1271 with the Aspro Gialoudi deposit and implications for the formation of the Milos
1272 manganese mineralization. Ore Geol., 80, 594–611, 2017.
1273 Paulmier, A., Ruíz-Pino, D., and Garçon, V.: The oxygen minimum zone (OMZ) off
1274 Chile as intense source of CO2 and N2O, Cont. Shelf. Res., 28, 2746–2756, 2008.
1275 Paulmier, A., Ruiz-Pino, D., and Gaçon, V.: CO_2 maximum in the oxygen minimum
1276 zone (OMZ). Biogeosciences, 8, 239–252. doi:10.5194/bg-8-239-2011, 2011.
1277 Percoits, E., Gingras, M. K., Barley, M. E., Kapper, A., Posth, N. R., and Konhauser,
1278 K.O.: Petrography and geochemistry of the Dales Gorge banded iron formation:
1279 Paragenetic sequence, source and implications for palaeo-ocean chemistry. Pre.
1280 Res., 172, 2009.

1281 Pichler, T. and Dix, G. R. Hydrothermal venting within a coral reef ecosystem,
1282 Ambitle Island, Papua New Guinea. Geology, 50, 435–438, 1996.
1283 Pichler, T. and Veizer, J.: Precipitation of Fe(III) oxyhydroxide deposits from
1284 shallow-water hydrothermal fluids in Tutum Bay, Ambitle Island, Papua New
1285 Guinea. Chem. Geol., 162, 15–31, 1999.
1286 Pichler, T. and Veizer, J. The precipitation of aragonite from shallow-water
1287 hydrothermal fluids in a coral reef, Tutum Bay, Ambitle Island, Papua New
1288 Guinea. Chem. Geol., 207, 317–45, 2004.
1289 Planavsky, N., Rouxel, O., Bekker, A., Shapiro, R., Fralick, P., and Knudsen, A.:
1290 Iron-oxidizing microbial ecosystems thrived in late Paleoproterozoic redox-
1291 stratified oceans. Earth Plan. Sci. Letts., 286, 2307–242, 2009.
1292 Planavsky, N. J., Bekker, A., Rouxel, O. J., Kamber, B., Hofmann, A., Knudsen, A.
1293 and Lyons T. W.: Rare earth element and yttrium compositions of Archean and
1294 Paleoproterozoic Fe formations revisited: New perspectives on the significance
1295 and mechanisms of deposition. Geochim. Cosmo. Acta, 74, 6387–6405, 2010.
1296 Plimer, I. Milos Geologic History. Koan Publishing House, Athens, Greece. 261 pp,
1297 2000.
1298 Poulton, S.W., and Canfield, D.E.: Development of a sequential iron extraction
1299 procedure for iron: implications for iron partitioning in continentally derived
1300 particles. Chem. Geol. 2014, 209–221, 2005.
1301 Poulton, S.W. and Canfield, D.E.: Ferruginous conditions: A dominant feature of the
1302 ocean through Earth's history. Elements. 7, 107–112, 2011.
1303 Preuß, A., Schauder, R., Fuchs, G., and Stichler W.: Carbon isotope fractionation by
1304 autototrophic bacteria with three different CO_2 fixation pathways. Zeitschrift für
1305 Naturforschung C., 44, 397–402, 1989.

Rancourt, D. G., Fortin, D., Pichler, T., and Lamarche, G.: Mineralogical characterization of a natural very As-rich hydrous ferric oxide coprecipitate formed by mixing of hydrothermal fluid and sea water. Am. Min., 86, 834–851, 2001.

Rasmussen, B., Meier, D. B., Krapež. B., and Muhling, J. R.: Iron silicate microgranules as precursor sediments to 2.5-billion-year-old banded iron formations. Geology, 41, 435–438, 2013.

Rasmussen, B., Krapež, B., and Meier, D. B. Replacement origin for hematite in 2.5 Ga banded iron formation: Evidence for postdepositional oxidation of iron-bearing minerals. Geol. Soc. Am. Bull., 126, 438–446, 2014.

Riedel, T., Zak, D., Biester, H., and Dittmar, T.: Iron traps terrestrially derived dissolved organic matter at redox interfaces. Proc. Nat. Acad. Sci. U.S.A., 110, 10101–10105, 2013.

Robbins, E. I., Kourtidou-Papadeli, C., Iberall, A. S., Nord, Jr, G. L. and Sato, M.: From Precambrian Iron-Formation to Terraforming Mars: The JIMES Expedition to Santorini. Geomicrobiol. J., 33, 630–645, 2016.

Roy, S.: Manganese Mineralization: Geochemistry and mineralogy of terrestrial and marine deposits. Geol. Soc. Spe. Pub., 119, 5–27, 1997.

Roy, S.: Sedimentary manganese metallogenesis in response to the evolution of the Earth system. Earth-Sci. Rev., 77, 273–305, 2006.

Rudnick, R. and Gao, S. Composition of the continental crust. In: Treatise on Geochemistry, vol. 3. Elsevier–Pergamon, Oxford, 1–64 pp, 2003.

Shanmugam, G.: Submarine fans: a critical retrospective (1950–2015). J. Palaeogeogr., 5, 110-184, 2016.

Schwertmann, U. and Murad, E. Effect of pH on the formation of goethite and hematite from ferrihydrite. Clay Clay Min., 31, 277–284, 1983.

1331 Shuster, D. L., Farley, K. A., Vasconcelos, P. M., Balco, G., Monteiro, H. S.,
1332 Waltenberg, K., and Stone, J. O. Cosmogenic 3 He in hematite and goethite from
1333 Brazilian “canga” duricrust demonstrates the extreme stability of these surfaces.
1334 Earth Plan. Sci. Lett., 329, 41–50, 2012.
1335 Sigurdsson, H., Carey, S., Alexandri, M., Vougioukalakis, G., Croff, K., Roman, C.,
1336 Sakellariou, D., Anagnostou, C., Rousakis, G., Loakim, C., Goguo, A., Ballas, D.,
1337 Misaridis, T., and Nomikou, P. Marine investigations of Greece’s Santorini
1338 volcanic field. EOS Trans. Am. Geophy. Union, 87, 337–342, 2006.
1339 Simonson, B. M.: Sedimentological constraints on the origins of Precambrian iron-
1340 formations. Geol. Soc. Am. Bull., 96, 244–252, 1985.
1341 Simonson, B. M. and Hassler, S. W.: Was the deposition of large Precambrian iron
1342 formations linked to major marine transgressions? The J. Geol., 104, 665−676,
1343 1996.
1344 Skarpelis, N. and Koutles, T.: Geology of epithermal mineralization of the NW part of
1345 Milos Island, Greece. In Proceedings of the 5th International Symposium on
1346 Eastern Mediterranean Geology. (eds. Chatzipetros, A. & Pavlides S). School of
1347 Geology, Aristotelian University of Thessaloniki, Thessaloniki, Greece. pp. 1449–
1348 1452, 2004.
1349 Smith, A.J.B., Beukes, N.J., and Gutzmer, J.: The Composition and depositional environments of
1350 Mesoarchean Iron Formations of the West Rand Group of the Witwatersrand Supergroup, South
1351 Africa. Econ. Geol. 108, 111-134, 2013.
1352 Sperling, E.A., Wolock, C.J., Gill, B.C., Kunzmann, M., Halverson, G.P., Macdonald,
1353 F.A., Knoll, A.H., and Johnston D.T.: Statistical Analysis of Iron Geochemical
1354 Data Suggests Limited Late Proterozoic Oxygenation. Nature 523, 451–454, 2015.

1355 Stewart, A. L. and Mcphie, J.: Facies architecture and Late Ploicene – Pleistocene
1356 evolution of a felsic volcanic island, Milo, Greece. Bull. Volcanol. 68, 703–726,
1357 2006.
1358 Sun, S., Konhauser, K. O., Kappler, A., and Li, Y.-L.: Primary hematite in
1359 Neoarchean to Paleoproterozoic oceans. GSA Bull., 127, 850–861, 2015.
1360 Stüben, D. and Glasby, G.P.: Geochemistry of shallow submarine hydrothermal fluids
1361 from Paleohori Bay, Milos, Aegean Sea. Exp. Min. Geol., 8, 273–287, 1999.
1362 Swamy, V., Saxena, S. K., Sundman, B., and Zhang, J.: A thermodynamic assessment
1363 of silica phase diagram. J. Geophys. Res. Solid Earth, 99, 11787–11794, 1994.
1364 Taylor, J., and Parkes, R. J.: The cellular fatty-acids of the sulfate-reducing bacteria,
1365 Desulfobacter sp., Desulfobulbus sp. and Desulfovibrio desulfuricans. J. Gen.
1366 Microbiol., 129, 3303–3309, 1983.
1367 Tice, M. M. and Lowe, D. R.: The origin of carbonaceous matter in pre-3.0 Ga
1368 greenstone terrains: A review and new evidence from the 3.42 Ga Buck Reef
1369 Chert. Earth Sci. Rev., 76, 259–300, 2006.
1370 Tiodjio, R. M., Sakatoku, A., Nakamura, A., Tanaka, A., Fantong, W. Y., Tchakam,
1371 K. B., Tanyileke, G., Ohba, T., Hell, V. J., Kusakabe, M., Nakamura, S., and Ueda,
1372 A.: Bacterial and archaeal communities in Lake Nyos (Cameroon, Central Africa).
1373 Sci. Rep., 4, 6151, DOI: 10.1038/srep06151, 2014.
1374 Trendall, A.F.: The significance of iron-formation in the Precambrian stratigraphic
1375 record. Int. Assoc. Sed. Spe. Pub., 33, 33–66, 2002.
1376 Tsikos, H., Mathews, A., Erel, Y., and Moore, J.M.: Iron isotopes constrain
1377 biogeochemical redox cycling of iron and manganese in a Palaeoproterozoic
1378 stratified basin. Earth Planet. Sci. Lett., 298, 125–134, 2010.

van Hinsbergen, D. J. J., Snel, E., Garstman, S. A., Mărunţeanu, M., Langereis, C. G., Wortel, M. J. R., and Meulenkamp, J. E.: Vertical motions in the Aegean volcanic arc: evidence for rapid subsidence preceding volcanic activity on Milos and Aegina. Mar. Geol., 209, 329–345, 2004.

Varnavas, S. P. and Cronan, D. S.: Submarine hydrothermal activity off Santorini and Milos in the Central Hellenic Volcanic Arc: A synthesis. Chem. Geol., 224, 40–54, 2005.

Weber, K. A., Achenbach, L. A., and Coates, J. D.: Microorganisms pumping iron: anaerobic microbial iron oxidation and reduction. Nat. Rev. Microbiol., 4, 752–64, 2006.

Table 1. Table 1. Results of X-Ray Radiation (XRD) analysis showing major mineralogical compositions. NFIF (non-fossiliferous iron formation) and MFIF (microfossiliferous iron formation), respectively.

Mineral phase	MFIF1	MFIF2	MFIF3	Fe-rich NFIF2A	Si-rich NFIIF2B	Fe-rich NFIF2C	Si-rich NFIFD	Fe-rich NFIF2E	Fe-rich NFIF2F
Hematite	+	+	-	+	+	+	+	+	+
Quartz	+	+	+	-	-	-	-	-	-
Sanidine	-	-	-	+	+	+	+	+	+
Tridymite	-	-	-	-	+	+	+	+	+
Cristobalite	-	-	-	+	-	-	-	-	-
Cryptomelane	-	-	+	-	-	-	-	-	-

Table 2. Stable isotope results. Letters A-F on the NFIF samples represent respective bands of the sawn rock in Figure 7E.

Sample	$\delta^{13}C_{org}$ vs PDB (‰)	C_{org} (%)	$\delta^{15}N$ vs air (‰)	N (%)	$\delta^{34}S$ vs CDT (‰)	S (%)
Fe-rich NFIF2A	-25,63	0,061	nd	0,023	nd	0,01
Si-rich NFIF2B	-25,03	0,109	nd	0,017	nd	0,02
Fe-rich NFIF2C	-24,45	0,068	nd	0,013	nd	0,02
Si-rich NFIF2D	-25,04	0,076	nd	0,015	nd	0,02
Fe-rich NFIF2E	-25,19	0,042	nd	0,009	nd	0,01
Si-rich NFIF2F	-25,49	0,050	nd	0,012	nd	0,03
MFIF1	-25,49	0,087	nd	0,017	nd	0,01
MFIF2	-26,25	0,046	nd	0,005	nd	nd
MFIF3	-25,69	0,041	nd	0,006	nd	nd

ND, Not detected

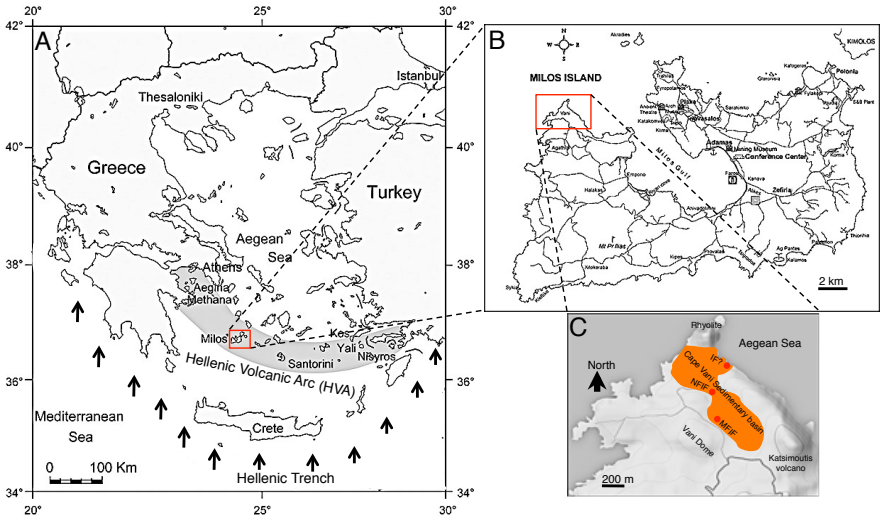

Fig. 1. Geological map of Milos (redrawn from Marschik et al., 2010). (A), Geotectonic map showing the position of Milos Island, along the Hellenic Volcanic Arc (HVA). Arrows indicate north east subduction of the African plate underneath the Euroasian plate. (B) Milos Island. (C), The Milos iron formation is located in the 8-shaped Cape Vani sedimentary basin (CVSB). At least two IFs are present in the CVSB. These are made up of a non-fossiliferous IF (NFIF) at the juncture between the two large sedimentary basins and a microfossiliferous IF (MFIF) located at the SW margin in the second basin. A potential third IF (IF?) is located to the NE, close to the present day Aegean Sea. It is however not certain if this deposit is part of the NFIF or not, because of the open mining pit separating the two.

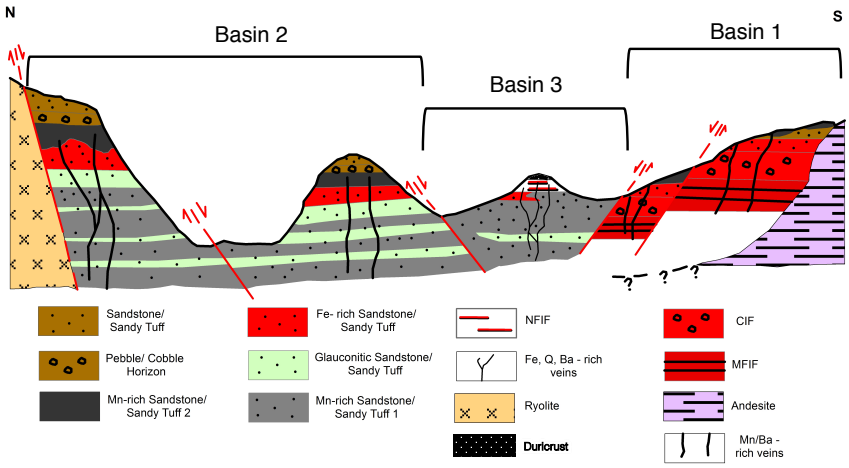

1477

1478 Fig. 2. A generalized north-south stratigraphic map of the ~1 km long CVSB showing
1479 interpreted geology, lithology, main faults and how they relate to the iron and
1480 manganese formations, in support of a three-basin hypothesis. Not drawn to scale.
1481 Four types of iron-rich sedimentary rocks occur in the CVSB. These include the iron-
1482 rich sandstones, the iron-Mn-rich sandstones, the conglomerate hosted iron formation
1483 (CIF) and the MFIF and NFIF formations that are depositionally and chemically
1484 distinct from the sandstone deposits.
1485

1486

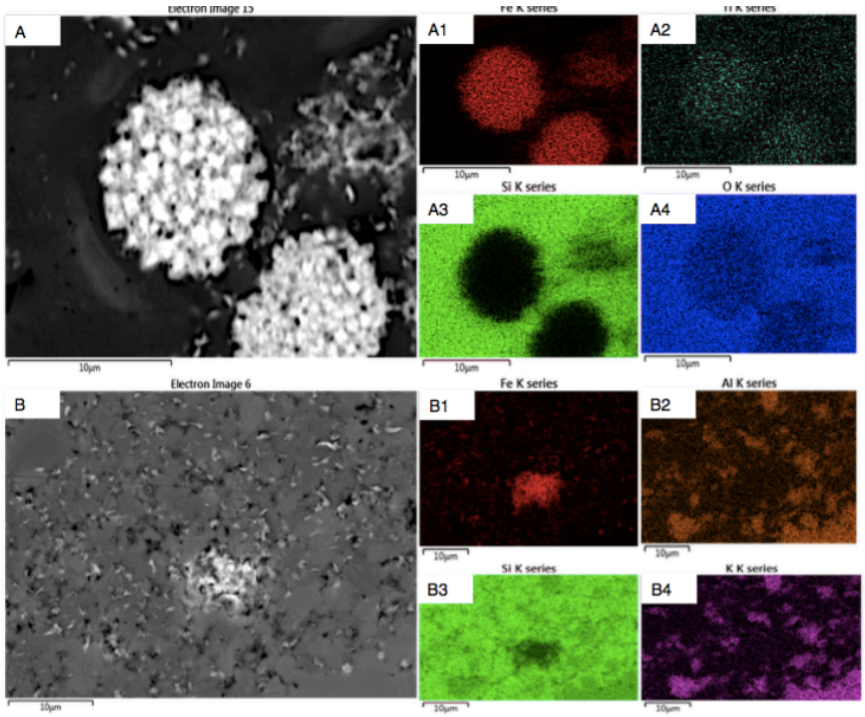

Fig. 3. EDS-electron micrograph showing Fe-rich mineral phases in a Si-rich matrix from the MFIF. The bright colours correspond to the analysed elements. (A), framboidal hematite particles. A1-A4, elemental compositions of the framboidal particles in A. (B), Dispersed fluffy Fe-rich mineral grains. B1-B4, corresponding elements associated with the micrograph in panel A

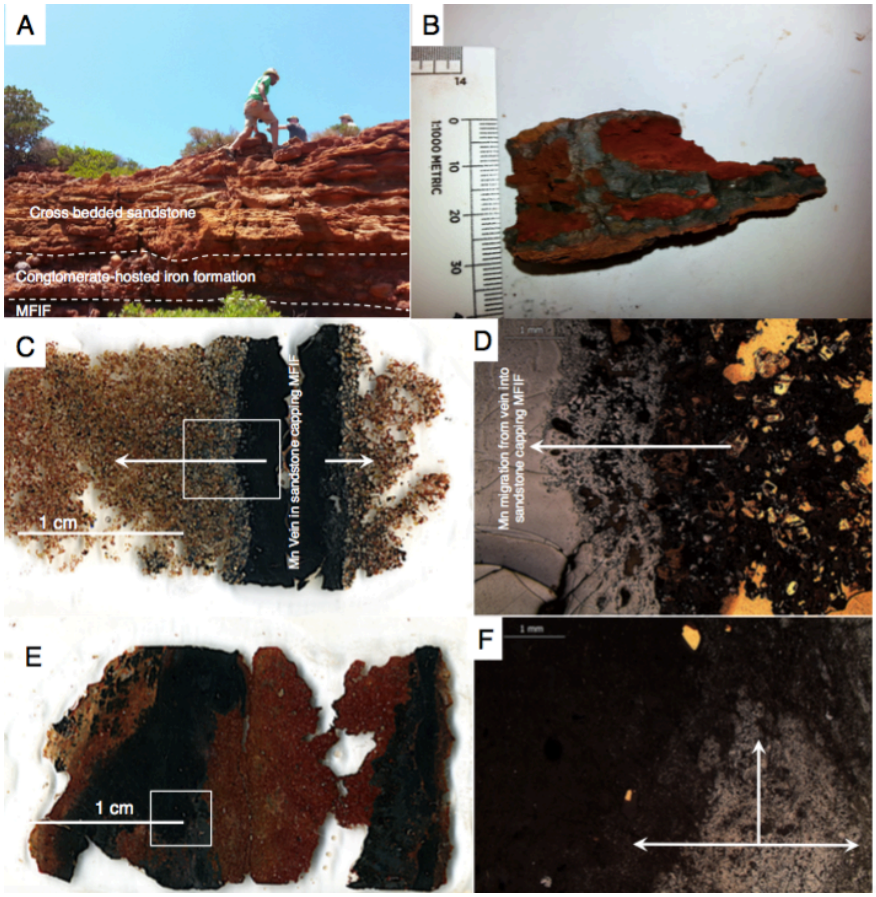

1494

1495 Fig. 4. Sedimentary profile, thin section scans and optical microscope images of the
1496 MFIF. (A), Field photo showing the sedimentary profile of the MFIF chacterized by
1497 the overlying sandstone cap. (B), Photograph showing black diffused Mn-rich bands
1498 near the base of the MFIF. (C), Scanned image of thin section showing a black Mn-
1499 rich vein in the overlying MFIF sandstone showing a gradient of Mn migrating into
1500 the sandstone matrix (white arrows). (D), Light microscopy images showing details in
1501 panel C. (E), Scanned image of an MFIF thin section showing black Mn bands
1502 migration into a red iron-rich background. (F), Amplified light microscope image
1503 showing gray Mn layers migrating into a black Fe-rich matrix. White arrows show
1504 direction of movement. Boxes in C and E are amplified in D and F.
1505

1506

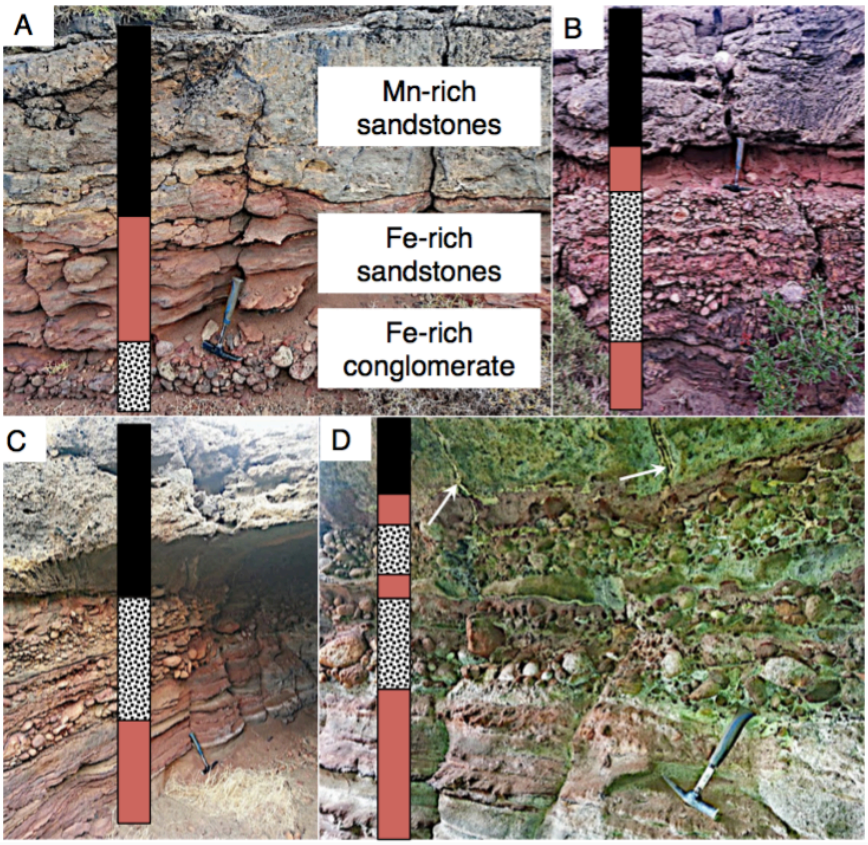

Fig. 5. Sedimentary sequence overlying the MFIF, consisting of thin (<0.5 m) polymictic andesite-dacite cobble-pebble, and sandstone-sandy tuff pebble, and Fe-rich conglomerate facies overlain by thinly laminated Fe-rich sandstone beds. This vertical sequence is interpreted to represent a progressively deeper water environment up the sequence (A), for reasons including sea level rise due to tectonic subsidence. The multiple cycles in B-D suggest potential episodes of sea level change. Arrows in D show hydrothermal feeder veins feeding the overlying layers. The sequence is overlain by a thin package of parallel and cross-bedded Mn-sandstone cap.

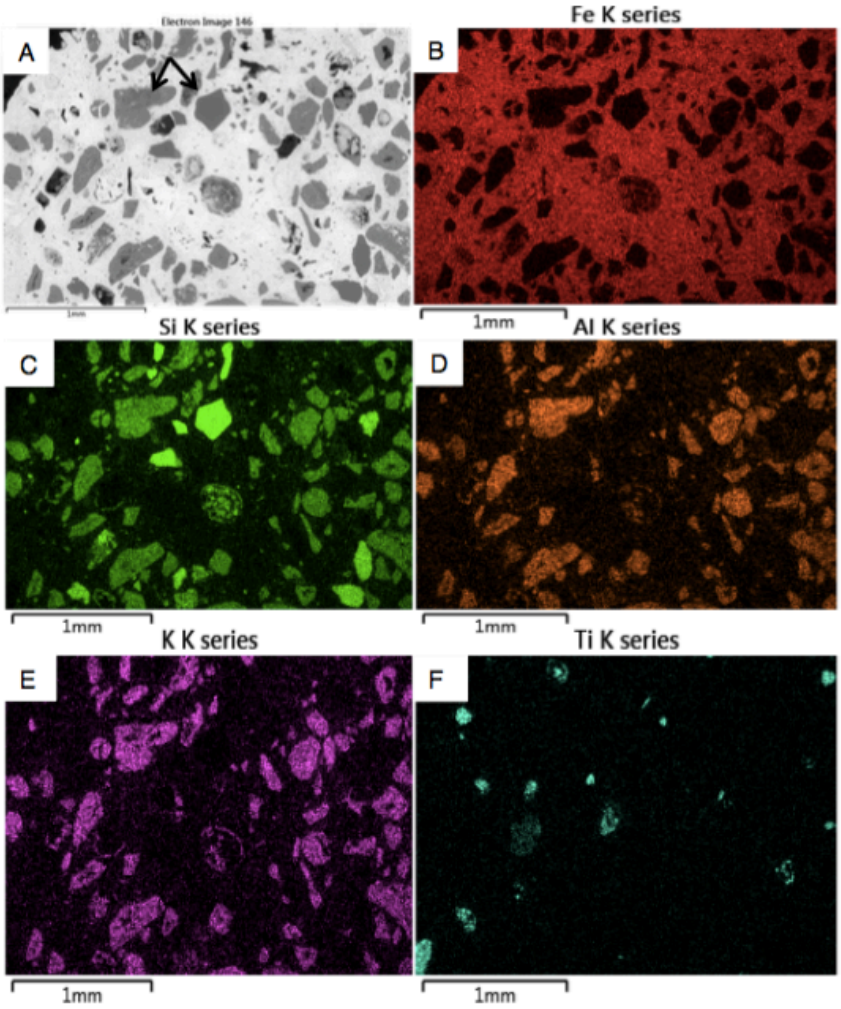

1518

1519 Fig. 6. Scanning electron microscope micrograph showing the chemical composition
1520 of volcaniclast (arrows in A) and the iron cement of the conglomerate hosted IF (CIF)
1521 overlying the MFIF.
1522

1523

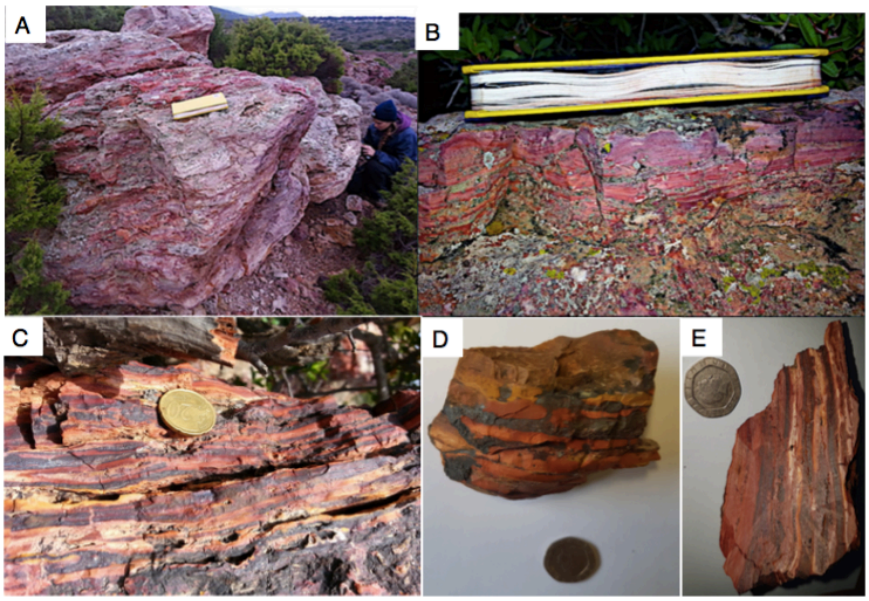

Fig. 7. Examples of the NFIF banded iron rocks. (A-C), Field photographs. (D), Handheld banded Fe sample. (E), Sawn NFIF sample with laminated Fe-rich bands alternating with Si-rich bands.

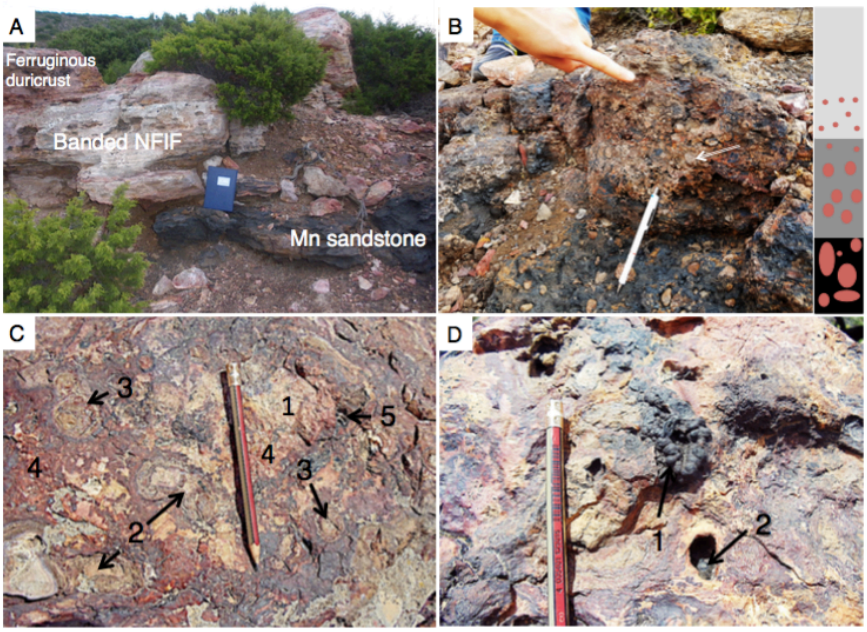

Fig. 8. Field sedimentology and stratigraphy of Section B sequence, host to the NFIF. (A), Sharp boundary between lower Mn sandstone and unconformably overlying NFIF capped by a ferruginous duricrust. (B), Sandstone-sandy tuff pebble to gravel conglomerate facies, showing an upward fining character, locally overlies the Mn sandstone bed and capped by a sharp erosional contact with the overlying NFIF. The tip of the pen (7 cm long) rests on late blue-black Mn oxide overprint. (C), Ferruginous duricrust made up of lithic fragments composed of (1) Fe-nodules (2) and Fe-concretions (3) in a hematite-rich matrix (4). (D), Matrix dissolution resulting in vermiform Mn nodules (1) and cavity black Mn oxide (2) infillings, post-dating the ferruginous duricrust formation.

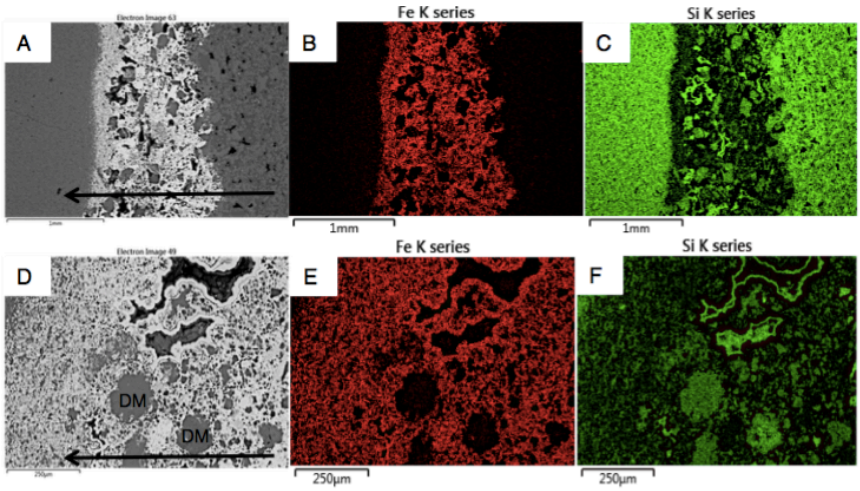

Fig. 9. EDS-electron micrograph showing major elemental composition of typical Fe bands alternating with Si-rich layers in the NFIF. Volcaniclastic detritus mostly present in the Fe-rich bands, suggests precipitation during active submarine volcanism. To the contrary, the Si-rich band grains that are of a homogenous fine size composition and lacking volcaniclast, suggest deposition during intervals of minimal volcanic activity. Arrows in A and B depict the direction of sedimentation, seen to proceed from an Fe-rich matrix mixed with large grains of volcaniclastic detritus (DM) to one composed essentially of very fine-grained Fe particles before transitioning into the very fine-grained Si-rich layer. An upward fining of the volcaniclastic particles in the Fe-rich layers transitions from one made up of volcaniclastic debris and hematite, to a mainly thin hematite-rich horizon at the top of this mixed layer (see supplementary Figs 8-11 for details). This concurrent occurrence of volcaniclast and Fe oxides, combined with the upward fining nature of the Fe-rich layers, suggest the release and oxidation of Fe(II) coincided with the settling of hydrothermal debris resulting from the introduction of enormous amount of reduced materials into the water column. The Fe-rich layer ceased forming as hydrothermal/volcanic release of Fe subsided, followed by deposition of the Si-rich layer. This repetitive cycle of events is observed for tens of metres laterally and vertically, stressing that the layers are not single isolated or post-depositional replacement events, but chemical precipitates that sequentially sedimented out of the water column. Red colour in B and C depict Fe and green in C and F, Si.

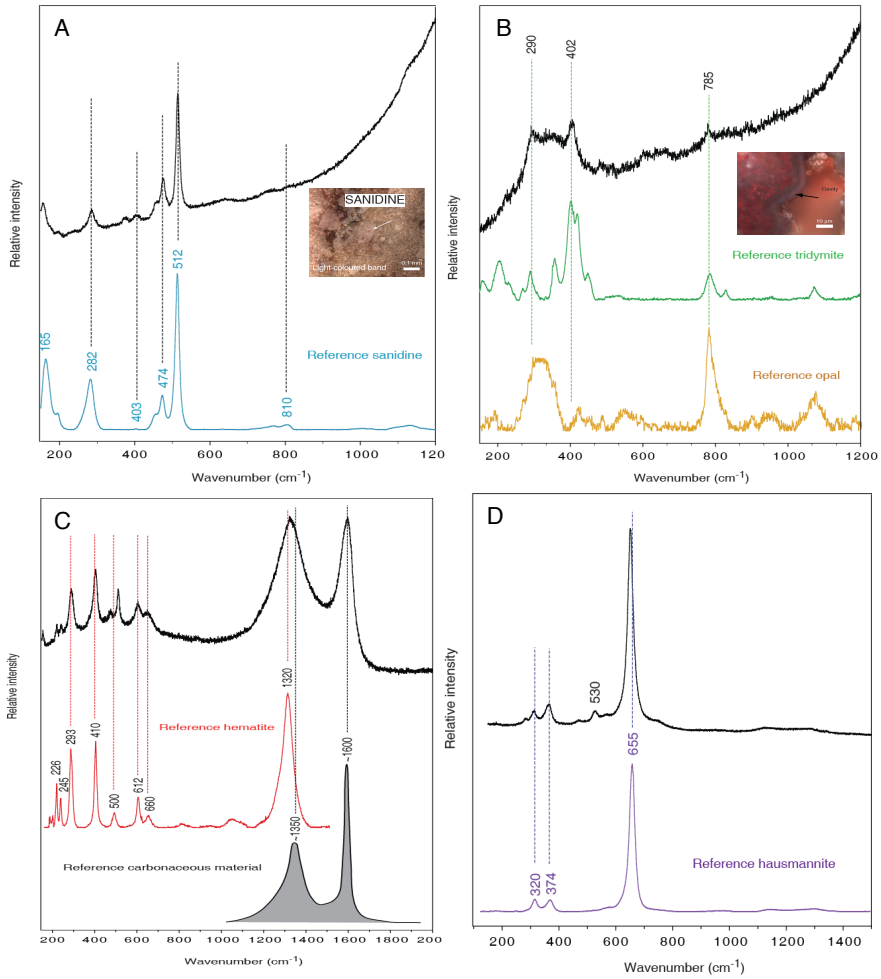

Fig. 10. Raman spectroscopy of the Fe-rich and/or Si-rich bands from NFIF.

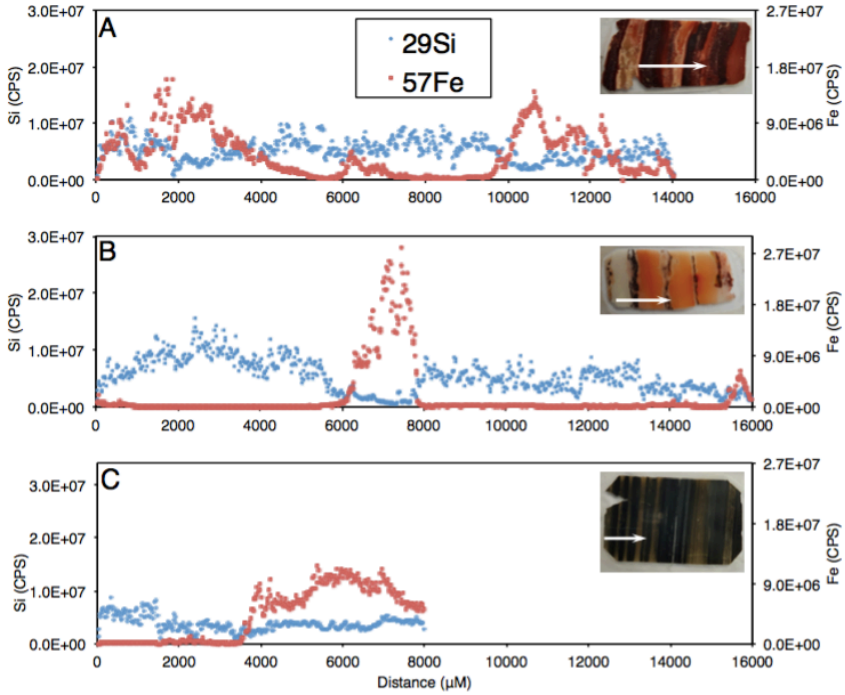

1570

1571 Fig. 11. Fluctuation in Si and Fe content measured by in situ laser ablation ICP-MS
1572 analysis. (A), Milos BIF-type rock with evenly distributed Si and Fe rich bands. (B),
1573 Milos BIF type rock with wide Si-rich (whitish-brownish strips) and narrow Fe-rich
1574 bands (dark strips). (C), An example for the 2.5 Ga Kuruman BIF. Insets are analyzed
1575 thin sections. For scale, each thin section is ≈3.3 cm long, in the direction of the
1576 arrows indicating the area analyzed.
1577

1578

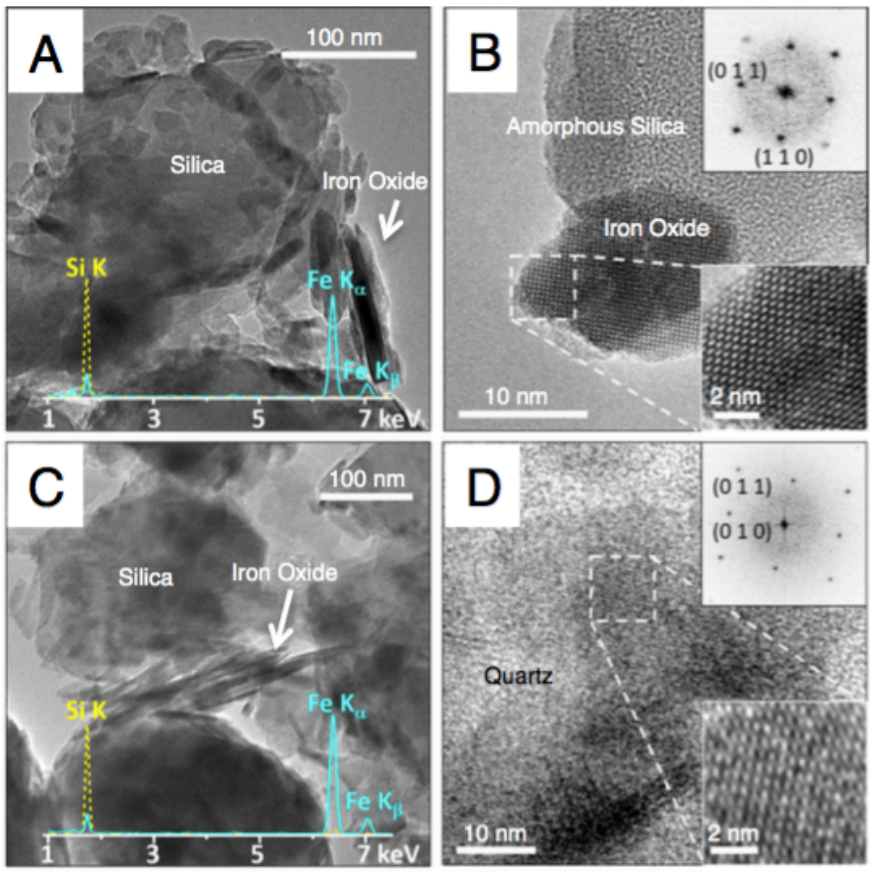

Fig. 12. TEM characterization of an NFIF and MFIF specimen. (A) lower magnification MFIF TEM-BF micrograph. (B) High resolution micrograph of NFIF showing amorphous Si and Fe oxide crystallline lattice structures. Insets highlight a hematite particle viewed from the [1-11] axis (Rhombohedral lattice). (C) Lower magnification MFIF TEM-BF image. (D) High resolution images of MFIF showing crystalline quartz and iron oxide crystallline lattice structures. Insets in (D) show a quartz crystal viewed from the [100] axis. Both samples contain silica with a few hundred nm particle size, and smaller needle-like iron oxide particles. Spectral lines in panels (A) and (C) are X-ray Energy Dispersive elemental profiles of the individual Fe and Si mineral phases.

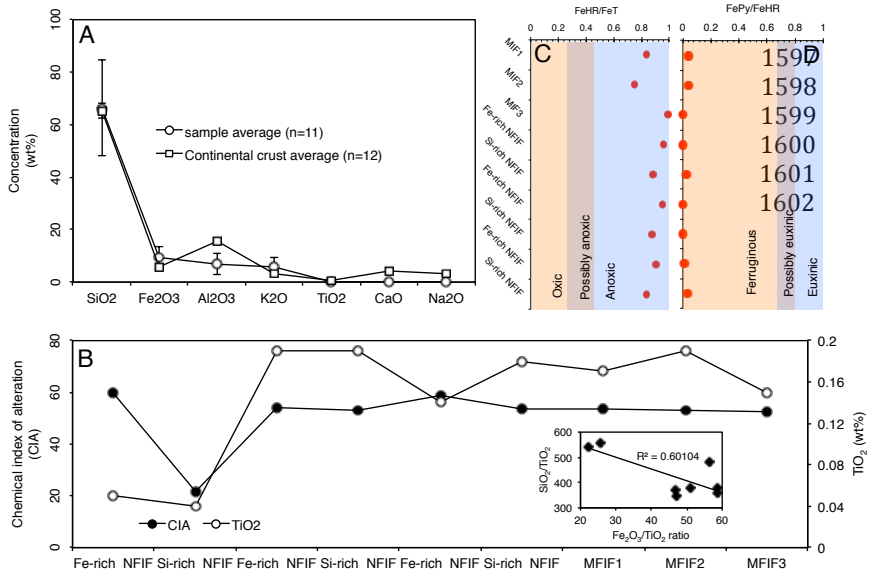

Fig. 13. Bulk average concentrations of major trace elements, chemical weathering indices and reconstructed redox depositional conditions for typical MFIF and the Fe/Si-rich NFIF ands for the sawn rock sample in Figure 7E. (A), Relationship between average major trace element content and average continental crust (Rudnick and Gao, 2003). (B), Chemical Index of Alteration (CIA). Inset, relationship between SiO_2 and Fe_2O_3. (C) Highly reactive Fe (FeHR) to Total Fe ratio (FeT). (D) Pyrite to FeHR ratio.

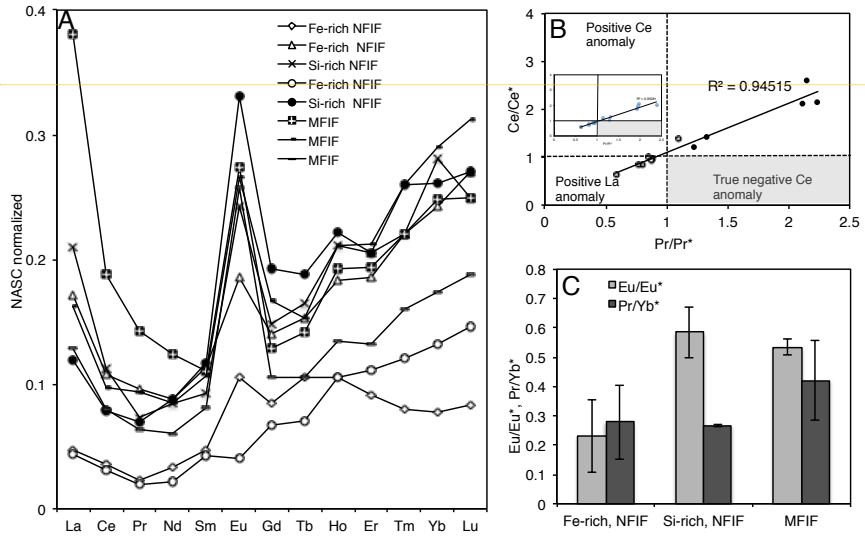

Fig. 14. Rare earth element (REE) distribution in samples and calculated Ce and Eu anomalies for NFIF bands and MFIF. (A), NASC normalized REE distribution in various rock facies. (B), Ce anomalies. (C), Eu anomalies and light REE (LREE) vs. heavy REE (HREE) ratio in the NFIF bands and MFIF. Similar trends were reproduced for Post Archean Australian Shale (PAAS) normalized REE (McLennan, 1989; Bau and Dulski, 1986), exemplified by the inset in B.

Unknown
Formatted: Font:(Default) Times New Roman, Font color: Text 1

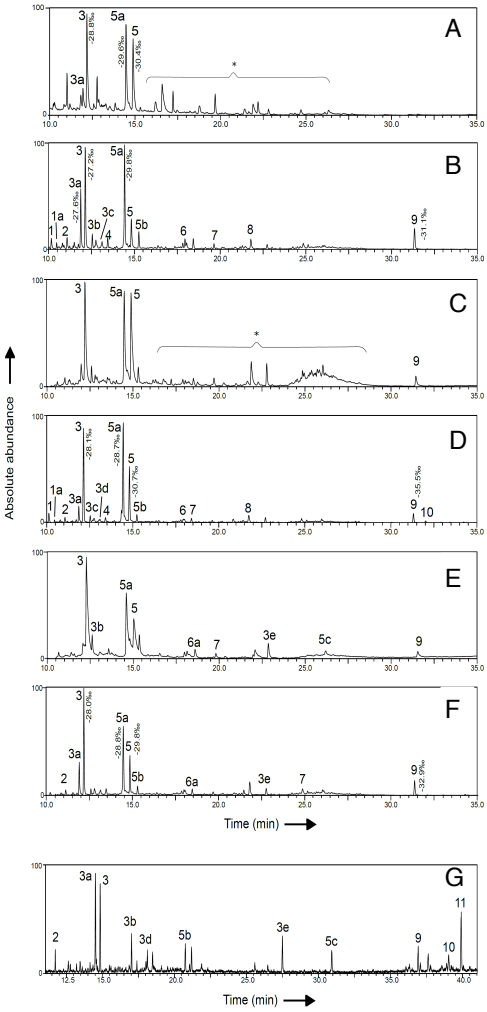

Fig. 15. GC/MS chromatogram sections of total lipid extracts of the BIF-type rocks (A-F). Data are for individual bands excised from the sawn rock in Figure 7E. Panel G illustrates total lipid extract for the modern shallow submarine hydrothermal sediments at Spathi Bay, south east on the coast of Milos Island. Peak values indicate the lipid-specific $\delta^{13}C$ values per mil. Because of the low intensity of the lipids recovered, it was not possible to obtain $\delta^{13}C$ values specific for all peaks. Peaks are annotated as; FAME = fatty acid methyl ester; Me = methyl group; TMS = trimethylsilyl; TMSE = trimethylsilyl ester. (1) $C_{14:0}$ FAME, (1a) $C_{14:0}$ 13Me FAME, (2) $C_{15:0}$ FAME, (3) $C_{16:0}$ FAME, (3a) $C_{16:9}$ FAME, (3b) C16:0 TMS, (3c) 10Me $C_{16:0}$ FAME, (3d) $C_{16:9}$ FAME, (3e) $C_{16:0}$ TMSE, (4) $C_{17:0}$ TMS, (5) $C_{18:0}$ FAME, (5a) $C_{18:9}$

FAME, (5b) $C_{18:0}$ TMS, (5c) $C_{18:0}$ TMSE, (6) $C_{19:0}$ FAME, (6a) $C_{19:0}$ 18Me TMS, (7) $C_{21:0}$ TMS, (8) $C_{22:0}$ TMS, (9) Cholesterol TMS, (10) Stigmasterol TMS, (11) beta-Sitosterol (*) contaminants (e.g., phthalates).

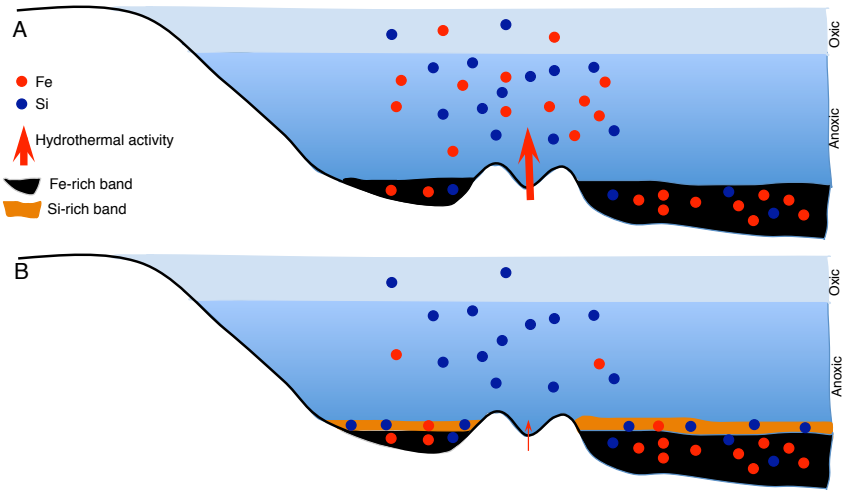

Fig. 16. Conceptual model of the mechanism of band formation of the NFIF, related to changes in the intensity of hydrothermal activity and chemical oxidation of Fe(II) to Fe(III) in the water column, inferred from the data. See Chi Fru et al. (2013) for a biological model for the formation of the MFIF.